Mechanisms of shear band formation in heterogeneous materials under compression: The role of pre-existing mechanical flaws

Manaska Mukhopadhyay[1,1], Arnab Roy[1,1], and Nibir Mandal[1,1]

[1]Jadavpur University

October 17, 2023

Abstract

Shear bands critically govern the shear failure processes and associated many geophysical phenomena, e.g., faulting, in Earth's crust. Earlier investigations on homogeneous materials recognized temperature and strain rate as the principal factors controlling the band growth. However, how inherent mechanical heterogeneities can influence their growth mechanism and internal structures remained unexplored. From plane-strain compression experiments on rock analogue models the present article addresses this issue. It is demonstrated from these experiments that mechanical heterogeneities dictate the failure to develop wide bands, localized preferentially in their neighborhood, unlike uniformly distributed, conjugate sets of closely spaced narrow bands in homogeneous models. The wide bands eventually attain a composite structure with a core of densely packed band-parallel sharp secondary bands, flanked by a linear zone of closely spaced, narrow bands. This study also reveals the effects of global strain-rate on the band evolution in heterogeneous systems. Decreasing strain rates replace the composite bands by well-defined homogeneous shear bands, containing a core of uniform shear, bordered by narrow zones of weak shear, grading into completely unstrained walls. Numerical modelling in a visco-elasto-plastic rheological framework under geological strain-rates is used to quantify the strain partitioning patterns in the heterogeneity-controlled transformation of spatially distributed narrow to localized, wide composite shear bands. The model simulations also reveal that increasing strain rates facilitates the bands to form clusters, instead of single wide bands. The article finally provides a set of field observations to demonstrate the importance of heterogeneity-driven band mechanics in interpreting macro-scale shear zones in geological terrains.

Mechanisms of shear band formation in heterogeneous materials under compression: the role of pre-existing mechanical flaws

Manaska Mukhopadhyay, Arnab Roy and Nibir Mandal*

High Pressure and Temperature Laboratory, Department of Geological Sciences, Jadavpur University, Kolkata 700032, India.

Abstract

Shear bands critically govern the shear failure processes and associated many geophysical phenomena, e.g., faulting, in Earth's crust. Earlier investigations on homogeneous materials recognized temperature and strain rate as the principal factors controlling the band growth. However, how inherent mechanical heterogeneities can influence their growth mechanism and internal structures remained unexplored. From plane-strain compression experiments on rock analogue models the present article addresses this issue. It is demonstrated from these experiments that mechanical heterogeneities dictate the failure to develop wide bands, localized preferentially in their neighborhood, unlike uniformly distributed, conjugate sets of closely spaced narrow bands in homogeneous models. The wide bands eventually attain a composite structure with a core of densely packed band-parallel sharp secondary bands, flanked by a linear zone of closely spaced, narrow bands. This study also reveals the effects of global strain-rate on the band evolution in heterogeneous systems. Decreasing strain rates replace the composite bands by well-defined homogeneous shear bands, containing a core of uniform shear, bordered by narrow zones of weak shear, grading into completely unstrained walls. Numerical modelling in a visco-elasto-plastic rheological framework under geological strain-rates is used to quantify the strain partitioning patterns in the heterogeneity-controlled transformation of spatially distributed narrow to localized, wide composite shear bands. The model simulations also reveal that increasing strain rates facilitates the bands to form clusters, instead of single wide bands. The article finally provides a set of field observations to demonstrate the importance of heterogeneity-driven band mechanics in interpreting macro-scale shear zones in geological terrains.

Keywords: shear band growth, polymer models, compression test experiments, mechanical heterogeneity, finite element modelling, visco-elasto-plastic rheology

Plain Language Summary

Most of the earlier theoretical and experimental investigations dealt with mechanically homogenous models to address the problem of shear band formation. However, geological terrains can hardly be treated as ideally homogenous continua due to the presence of various mechanical heterogeneities, e.g., inherent fractures, melt pockets and contrasting lithological bodies. Using analogue laboratory experiments on heterogeneous polymer models this study demonstrates the role of pre-existing weak flaws in determining the modes of shear band formation (uniformly distributed, numerous narrow shear bands versus isolated, wide composite shear bands) under compression. The composite bands develop a characteristic internal structure, comprising a cluster of finely spaced narrow bands in the core, and regularly spaced orthogonal bands in the marginal zones. The experiments also reveal strain rate as a critical factor in determining the shear band structure in heterogeneous models. Reducing strain rate results in transformation of flaw-controlled band mechanisms: composite shear bands to homogeneous shear bands without any fine scale banding either in their core or margins. The article presents real-scale numerical simulations, the results of which support the experimental findings. A set of field examples is provided to highlight the geological relevance of flaw-controlled shear band mechanisms.

1. Introduction

Shear bands are typical manifestations of shear failure processes that play a critical role in accommodating differential displacements at plate boundaries to facilitate tectonic activities in Earth's crust, and trigger a range of important geophysical phenomena, such as faulting and earthquake generations. The mechanism of shear band formation is thus a subject of great interest in solid earth geophysics, with a special focus on the problem of strain partitioning in crustal deformations as a function of various physical factors and tectonic environments. Geological observations show that shear localization in rocks under crustal pressure-temperature conditions accommodate a large amount of plastic creep in a heterogeneous manner and produce a complex architecture, characterized by arrays of multiple shear bands (Mancktelow & Pennacchioni, 2005; Meyer et al., 2017; Rogowitz et al., 2016; Scholz & Choi, 2021; Snyder & Kjarsgaard, 2013; Vauchez et al., 2012). These bands generally show a wide variation in their geometry, displaying narrow and sharp to wide and diffused boundaries (Giorgio Pennacchioni & Mancktelow, 2007; Roy et al., 2022). In a geological terrain they usually occur as a complex system with their varying spatial densities, e.g., uniformly distributed numerous (Katz et al., 2004) to a few localized shear zones/bands (Fusseis & Handy, 2008). The geometrical and spatial diversity is reported from various geological settings, irrespective of their rock types, such as granites, sandstone and carbonates (Fossen et al., 2007; Gapais, 1989; Misra & Mandal, 2007). Some of the recent studies have recognized a number of specific geometrical patterns, e.g., anastomosing network (Finch et al., 2022; Fusseis et al., 2006), paired parallel arrays (Pennacchioni & Mancktelow, 2018), and branching dispositions (Meyer et al., 2017). Understanding the origin of such diverse shear band geometries and their controlling factors is a challenging issue in tectonic deformation studies.

The primary factors controlling the evolution of shear bands have been explored in multiple directions, aided with geological field investigations (Carreras et al., 2010; Ghosh & Sengupta, 1987) , laboratory experiments (Bowden & Raha, 1970; Camwell & Hull, 1973; Nizolek et al., 2021; Reber et al., 2020; Zielinski & Ast, 1983) and numerical simulations (Duretz et al., 2019; Finch et al., 2020; Roy et al., 2021). For example, Bowden and Raha's (1970) experiments on polymers, e.g., polystyrene (PS) and polymethyl methacrylate (PMMA) recognized temperature (T) and strain rates ($\dot{\varepsilon}$) as crucial factors to determine the mechanism of shear band localization in solids by plastic yielding under compression. Their PS experiments at a low temperature (T = 21°C) and high strain rate 2.3 x 10^{-2} s^{-1} produced numerous sharp micro shear bands of ~1µm thickness, which were replaced by a few wide, diffused shear bands at a higher temperature (T = 70°C) or lower strain rate ($\dot{\varepsilon}$: 6 x 10^{-3} s^{-1} to 4 x 10^{-3} s^{-1}) conditions. Several workers have used a range of other materials, such as steel and rocks in experiments and demonstrated varying band orientations with changes in both temperature and strain rates (Anand & Spitzig, 1980; David L. Kohlstedt & Holtzman, 2009). The mechanics of band formation turns to be more complex in geological settings due to involvement of several additional factors, such as pore fluid pressure, synkinematic rheological transformations on geological time scales and time-dependent rheological complexities. To deal with such geological problems, geoscientists have developed a range of numerical models on geological time scales (Gerya & Yuen, 2007; Meyer et al., 2017; Popov & Sobolev, 2008; Roy et al., 2021; Willis et al., 2019). A comprehensive review of these studies is provided in Regenauer-Lieb & Yuen, (2003).

The studies discussed above, mainly focused on temperature, strain rate and other geological factors controlling shear band formation in homogenous medium. Geological terrains, however, hardly behave as homogeneous continua as they usually contain inherent compositional or mechanical heterogeneities on macro- (e.g., igneous intrusives, faults or fracture zones, localized melt pockets, xenoliths) to microscopic (e.g., intragranular fractures/cracks, soft mineral aggregates, strong xenocrysts) scales. Field evidences suggest that such heterogeneities largely influence the locations of shear bands in naturally deformed rocks (Grujic & Mancktelow, 1998; Pennacchioni & Mancktelow, 2007). Laboratory experiments also reveal their effects in determining the location as well as the orientations of shear bands nucleated preferentially in the vicinity of mechanical flaws, such as, voids and rigid inclusions (Misra & Mandal, 2007). Several numerical studies have also shown similar heterogeneity effects on shear localization in geological settings (Gerya & Yuen, 2007; Kaus, 2010; Lemiale et al., 2008). However, none of the studies discussed above delved much into the complex internal architectures of bands evolved under the influence of mechanical imperfections in a continuum, which constitutes the main theme of the present work.

We conducted strain-rated controlled compression experiments on polystyrene (PS) sheets that under room temperature laboratory condition reproduced the typical plastic creep behaviour of common rocks reported from rock deformation experiments at elevated temperatures and pressures (Holtzman, Groebner, et al., 2003; Holtzman, Kohlstedt, et al., 2003; David L. Kohlstedt & Holtzman, 2009). From these experiments we demonstrate how pre-existing mechanically weak flaws can control the shear band mechanisms (numerous, sharp and narrow to composite wide band formation) in heterogeneous rock-analogues. We also present crustal scale numerical simulations within a framework of visco-elasto-plastic rheology which helps us to constrain the intermediate stages of deformation and provide a first-order quantification of accumulated strain and their corresponding strain partitioning behavior. Our experimental findings motivated us to look for similar shear band structures in natural rocks. We chose the Chotanagpur Granite Gneissic Complex (CGGC) terrains containing mylonite-bearing shear zones in granite hosts to compare our experimental results with the field observations. The article thus, finally discusses different types of shear band structures and their probable origin in the light of our laboratory experiments. This study provides a realistic mechanical model that explains the mechanism of shear band evolution with complex geometries and their spatial distributions commonly encountered in geological terrains.

2. Laboratory experiments

2.1. Experimental approach

Compressional test experiments (Fig. 1a) were conducted on polystyrene (PS) blocks (Fig. 1b) to study the mechanisms of shear band formation in laboratory conditions. PS was chosen our rock analogue, as it exhibits closest rheological similarity with shallow to mid crustal granitic terrains. We compared several physical properties like young's modulus, yield point, plastic creep behaviour and shear band angle of granite and other commonly found crustal rocks at elevated temperature with that of PS at room temperature and found similar rheological behaviour in both (details in Supplementary S1). Commercial grade PS also produced sharp shear bands under our experimental conditions (room temperature and strain rates). A 9 mm thick, rectangular (60 mm x 35 mm) block was cut out from a large PS sheet, and its vertical face was drilled to create a through-going cylindrical hole of ~1mm diameter, as illustrated in Fig.1b. We then filled the hole with commercially available epoxy with an intention to replicate the secondary filling materials, as found in geological cavities and fractures. An epoxy of extremely low yield strength (~7 MPa), compared to that of PS, was chosen to reproduce the mechanical setting of a weak flaw in the host. The models were left undisturbed overnight to allow the epoxy inside the hole to set in and form a mechanically weak solid region. The hole-normal vertical faces of the PS model were polished by P80 grit sandpaper to minimize the contact friction between the model block and the metal jig (Fig. 1a). We gridded the vertical faces by passive 2 mm × 2 mm square marker grids to visualize the macro-scale heterogeneous strain fields around the hole in the deformed sample. Models were deformed under a hydraulically driven compression machine (Aimil Hydraulic Press, with 1200kN load frame), equipped to control the strain rate during an experimental run by a flow-controlled valve. We developed a specially designed sample housing system (jig) (Fig. 1a) to run the deformation under a plane strain condition. The model was placed in the jig, keeping the flaw axis normal to the jig walls, and compressed with a vertical load (σ_1) under a biaxial stress condition, allowing the model to stretch perpendicular to the flaw axis (direction of no strain). To minimize the jig friction, we applied grease (viscosity 115 Pa s) at the model-jig wall interface prior to the beginning of model deformation. The experiments were run at ambient pressure and temperature (~27°C), keeping the σ_2 and σ_3 axes in horizontal directions, where σ_2 was oriented along the flaw axis direction (Fig. 1b). The vertical load (σ_1) was applied to the jig by moving the load frame in the upward direction against the stationary piston at the top, and continuously tracked by the 1200kN load cell attached at the top of the load frame. Under a given strain rate we ran a set of experiments for varying finite strains (6%, 12% and 18%) to study the progressive shear band structures with increasing deformation. Figure 1c shows the plastic creep behavior of PS at slow ($2x10^{-5}$ s^{-1}) and relatively fast strain rates ($3x10^{-5}$ s^{-1}). The material yields at a stress of ~130 MPa at the low strain-rate, whereas at ~150 MPa at the high strain-rate under the ambient temperature condition (27^oC). PS samples containing circular mechanical flaws reduce their yield stresses to ~95 MPa and ~110 MPa at low and high strain rates, respectively (Fig. 1c). We prepared the entire batch of PS models from the same PS sheet to avoid the possibility of any inherent variations in their rheological properties, e.g., yield strength, depending on the manufacturing history of the polymer. The reproducibility of our experimental results, e.g., plastic yielding in PS models, were tested by repeating each experiment several times (8 to 10) under the given condition.

To study the role of pre-existing heterogeneity in shear band development, we first ran a set of reference experiments on homogeneous PS models (devoid of induced cylindrical flaw) and compared the results with those obtained from heterogeneous models. Both the homogeneous and the heterogeneous model experiments were conducted at low ($2x10^{-5}$ s^{-1}) and high ($3x10^{-5}$ s^{-1}) strain rates, with an aim to explore the possible effects of deformation rates on the mechanism of flaw-controlled shear band localization. Our compression experiments occasionally produced tensile fractures in the models during the sample unloading, which was minimized by keeping the PS model inside the jig and allowing the hydraulic pressure to release at an extremely slow rate ($2x10^{-3}$ mm s^{-1}). After the successful unloading process, the model was cleaned and its vertical faces parallel to the σ_1-σ_3 plane were photographed to record the deformation patterns in the model, revealed from the deformed grids. The deformed specimens were cut into thin slices (~0.5mm thick), perpendicular to the flaw axis, and then mounted on a glass slide. The thin section was observed under cross-polarized light to study the shear band patterns, characterized by their strong optical birefringence (details on birefringence provided in Supplementary S2).

2.2. Experimental results

The PS model experiments produced three distinct types of shear band structures: narrow bands, wide composite bands and wide homogeneous bands (Fig. 2). Narrow bands are defined by their extremely long, narrow band geometry with sharp boundaries (Fig. 2a). They occur as densely penetrative band structures in a homogeneous medium. The presence of a mechanical heterogeneity results in a transition of the shear localization mechanism to form either composite bands or homogenous bands, depending on the bulk strain rates ($\dot{\varepsilon}$). A composite bands consists of two orthogonal sets of narrow bands, forming a composite structure: core (cluster of densely packed, sub-parallel narrow bands that accommodates maximum plastic strain) and transition zones (set of closely spaced orthogonal narrow bands showing shear drags) (Fig. 2b). A homogenous band, produced relatively at lower strain rate, is characterized by a thick band of homogenous shear localization, bounded by narrow zones showing gradational shear boundary with the walls (Fig. 2c). Detailed descriptions of these three different types of shear band formation are presented below .

2.2.1. Homogeneous models

Homogeneous PS models, deformed under high strain rates ($3x10^{-5}$ s^{-1}), produced numerous closely spaced, narrow shear bands, distributed more or less uniformly in the entire model region. Each band characteristically had geometrically exceptionally large lengths (L), small widths (W) with $L/W > 25$, and is defined by sharp boundaries (Fig. 3a). The narrow bands form typically in conjugate sets (Fig. 4a-i), with their dihedral angles (Φ) varying with increasing finite strain (ε). For $\varepsilon \sim 6\%$, the modal Φ lies in the range 70°-75°, which increases to ~80°-85° for $\varepsilon \sim 12\%$, and to ~85°-88° at $\varepsilon = 18\%$ (Fig. 4a-ii). Another interesting observation is that this type of bands multiplies in number to increase their areal density (Mauldon et al., 2001) (from $< 4 \text{ X } 10^{-3}$ mm^{-2} at 6% to $18 \text{ X } 10^{-3}$ mm^{-2} at 18%), with progressive compressional strains. To study such a spatio-temporal band evolution, we prepared band density maps from deformed models corresponding to $\varepsilon \sim 18\%$ (Fig. 4a-iii), and found the following features: 1) the bands do not cluster in specific zones; they are more or less homogeneously distributed; 2) progressively increasing new band formation facilitates the degree of homogeneity; and 3) at large finite strains it is hard to recognize individual bands as the band density is extremely high. For large $\varepsilon > 18\%$, the PS model produced a few isolated domains that accommodated plastic strains in the bulk model, forming shear zones at a high angle to the compression direction (Fig. 3a-iii).

Homogenous PS models deformed under lower strain rates ($2x10^{-5}$ s^{-1}) produced similar shear band geometry, implying that strain rate does not affect the mode of shear band growth in case of homogenous media. Detailed description is provided in Supplementary S3.

2.2.2. Heterogeneous models

Heterogeneous model experiments produced band structures markedly different from those formed in homogeneous models, irrespective of the strain rate ($\dot{\varepsilon}$) and the amount of finite strain (ε). However, $\dot{\varepsilon}$ critically controlled the mode of shear localization in the neighborhood of mechanical flaws, which we discuss later. Compression under high strain-rates ($\dot{\varepsilon}$ = 3 x 10^{-5} s^{-1}) developed plastic strains in the form of wide shear bands that localized preferentially at the extensional faces of a single pre-existing heterogeneity (Supplementary Fig. S4). These plastic zones contained numerous narrow shear bands in conjugate sets (Fig. 4b-i) with $\boldsymbol{\Phi}$ = ~ 98° (Fig. 4b-ii), forming a composite shear band structure (Fig. 3b). In a composite band one set of narrow band formed nearly parallel or at low angles (θ = ~ 10° - 15°) to the overall composite band trend, whereas the other at high angles (~ 85° - 95°), almost orthogonally oriented to it. Interestingly, the two sets had competing growth in the composite shear band evolution; the low-angle set increased its band density by multiplying the number of narrow bands and at the same time grew in length to form a well-defined core zone, which was practically devoid of high-angle shear bands. Such a differential narrow band growth gave rise to a characteristic two-layer composite band structure: a core zone of low-angle bands, flanked by zones of high-angle bands (called *transition zone* in the foregoing description). The transition zones represent an intermediate region between the strongly sheared core and the strain-free walls (revealed from weak or no optical birefringence and sharp termination of orthogonal narrow bands). Both the core and the transition zones increase their narrow band densities and formed a well-developed composite band structure at large ε (= 18%). A composite band eventually shows a complete segregation of the two band populations in the core and the transition zones, which is revealed from the band density map (Fig. 4b-iii). Composite shear bands had a lateral growth of their core zone at the cost of the transition zones, but they hardly change their overall band thickness. The core-zone grew in thickness with progressive deformations, e.g., 0.449 mm to 0.634 mm and finally to 0.949 mm at ε= 6%, 12%, and 18% of model strain, respectively, whereas the transition-zone underwent reduction in thickness at the same time, e.g., 0.667mm, 0.641mm, 0.556mm corresponding to these model strains. Consequently, the composite shear band structure persistently gained larger thickness ratios (T_r) between the core and transition zones with deformation, for example, T_r = 0.336 and 0.853 at ε= 6% and 18%, respectively.

To describe the overall band structure of a heterogeneous polystyrene model under high strain rates ($\dot{\varepsilon}$ = 3 x 10^{-5} s^{-1}), each circular heterogeneity localizes a conjugate pair of composite bands, symmetrically oriented at an angle of ~35° to the compression direction. Their core zones do not exactly follow the trend of composite band, but consistently form an oblique relation at an angle (θ) of ~10° to 15° (Fig. 2b). They have dihedral angles (~75°), significantly lower than that of the corresponding composite band (~93°). As the loading progresses, the circular flaw is deformed into an oval shape and the bands increase their dihedral angles by ~6°- 8°. The degree of shear partitioning between the core and transition zones of a composite shear band, calculated from the orthogonal narrow bands deflections (method of calculations elaborated in Supplementary S5), suggests contrasting shear localisation in the two domains of the shear band. For a given model compression, e.g., ε= 6%, the estimated shear in the core is ~0.72, which becomes extremely low (~0.11) in the transition zone. However, the transition zones progressively increase their shear at a large finite deformation (ε= 18%), e.g. their estimated shear is ~0.31 when the finite shear at the core is ~1.2.

Under a low compression rate (2×10^{-5} s^{-1}) the same heterogeneous PS model produced a symmetrical pair of nearly tabular conjugate bands, radiating from the heterogeneity at an angle of ~40° to the compression direction (Fig. 3c). In contrast to composite bands, they are completely devoid of narrow bands, and develop distributed plastic strains, giving rise to the characteristics of homogeneous shear bands. Secondly, their dihedral angle (Φ = ~80°) is lower than those of the composite bands. They have a narrow transition zone (T_r = ~0.3mm), revealed from the birefringence bands, on either side of the homogeneous core. The birefringence variations across the band length suggest a diffused boundary of the transition zone with the unstrained walls (Fig. 3c-iii). Models at increasing ε from 6% to 18% show little modifications in the homogenous bands, implying that they do not grow in thickness with increasing ε. Similarly, their transition zones remain unchanged, allowing the core zone to entirely accommodate the plastic strain in the model.

3. Numerical modelling

3.1. Theoretical considerations

Analogue models presented in the above section, represent the rheological setting of granitic crustal materials at temperatures of 500 – 800ºC, as discussed in detail in Supplementary (S1). However, the laboratory experiments could be used for qualitative measurements of the strain localization as a function of mechanical heterogeneities. Secondly, there was little scope for studying the entire spectrum of progressive shear band development in a test run. To overcome these experimental limitations, we use numerical modelling approach for a quantification analysis of strain localization and progressive band growth, considering the scales of physical model parameters applicable to upper to middle crustal conditions. We develop 2D finite element (FE) models to study the mechanisms of shear band localization as a function of mechanical heterogeneities based on nature-scaled parameters, with an aim to compare and provide a first-order quantification of the laboratory interpretations for geological strain rates. The FE modelling uses the open-source, particle-in-cell, finite element code *UNDERWORLD2* (http://www.underworldcode.org/) that solves the incompressible Stokes equations in combination with the energy conservation equation (Mansour et al., 2020; Moresi et al., 2007). We choose a rheological model, represented by a combination of an elastic (spring), a plastic (frictional block) and a viscous (dashpot) element in series (Fig. 5b).

We develop the finite element (FE) model on a rectangular domain in a Cartesian space, subjected to pure shear deformation (Fig. 5a), as in the laboratory setting. The model domain is discretized into quadrilateral meshes, comprising 564 x 328 elements. An elaborate description of the governing equations, numerical parameters and their constitutive relationships is given in Appendix A. We performed mesh refinement tests to find the level of mesh resolution required to attain a steady model output, implying that the simulation results hardly changed with further mesh refinement (detailed analysis in Supplementary S6). All numerical parameters are summarized in Table 1.

3.2. Shear band simulations

We performed three different sets of numerical simulations: 1) Model Simulations (MS1) to reproduce the reference laboratory experiments with homogeneous PS models; 2) Model Simulation (MS2) to replicate heterogeneous laboratory model containing a circular cylindrical flaw at high strain rates ($\dot{\varepsilon}$ = 2 x 10^{-12} s^{-1}), and 3) Model Simulation (MS3) similar to MS2, but run at a significantly low strain rates ($\dot{\varepsilon}$ = 5 x 10^{-14} s^{-1}). Figure 5c presents the typical stress-strain curves obtained from these three kinds of model simulations run at room temperature, where all of them show the stress to rise with increasing finite strain and reach the maximum yield stress, followed by a drop to the lower yield stress. This stress variation broadly agrees with the laboratory findings. The simulated models start to produce narrow shear bands at finite strains of about 3% - 4%, which commences prior to a proportionality limit of the stress-strain curve. However, narrow bands appear in large density only when the upper yield stress is attained at about 6% -7% strain. Sporadic narrow bands that initiated at a pre-upper yield stress might have resulted from local stress concentrations due to some mesh configurations.

MS 1: The homogeneous model initially (ε = ~4%) produced two sets of narrow shear bands, symmetrically oriented to the compression direction with a dihedral angle (Φ) of ~70°. They do not cluster in specific locations, but show a uniform spatial distribution in the model domain. They grow in length and at the same time, multiply in number to increase their spatial density with increasing ε (Fig. 6a). We calculated strain profiles along a number of transects in the simulated band structures to find the spatial patterns of band distributions (Fig. 6a-i). A profile for ε = 5% does not show any peaks (Fig. 7a-i), i.e., strain perturbations by shear band formation. In an advanced stage (ε > 10%) the simulation produces numerous peaks that amplify with increasing ε, but remain in low amplitudes (Fig. 7a). Their spatial patterns suggest a distributed development of band structures in the model simulations at ε = 15 – 20% (Fig. 7a-iv). However, a few bands selectively localise larger plastic strains, and gain prominence in the matrix of homogeneously distributed numerous bands. The shear bands hardly widen with progressive deformations.

MS 2: This simulation run at a higher strain-rate generates a pair of composite shear bands, radiating from the flaw boundary at a model strain (ε) < 5% (Fig. 6b). The shear bands are symmetrically oriented at an angle of ~40° to the compression direction, forming Φ ~ 80°. A close view of the model reveals a characteristic internal structure of the conjugate bands, each of them forms a narrow core zone of the greatest plastic strains, oriented obliquely to the overall band trend, as observed in composite bands of the laboratory experiments (Fig. 6b-iii). Two core zones on either flank of the flaw thus form a dihedral angle ($\Phi \sim 75°$) lower than that described by the overall conjugate band structures. They continue to accumulate plastic strain, leaving the rest part relatively unstrained. This model shows partitioning of the plastic strain equally into two parallel pairs of identical bands. Strain profile across the model (Supplementary S7) shows four distinct and almost equal peaks which demonstrates that the plastic deformation is accommodated into several bands (~4) of equal intensity.

MS 3: The simulation at a low model strain rate produces a pair of conjugate shear bands (Φ~75°) that localize preferentially at the extensional flaw boundary when ($\varepsilon < 5\%$) (Fig. 6c-i), as manifested in two high-amplitude, sharp peaks in the corresponding strain profile (Fig. 7). The time series simulations reveal that each shear band grows in length and concurrently multiplies the magnitudes of their maximum strain localization, eventually to form a core of homogeneously distributed strain, as observed in experimental homogenous bands. Such a band evolution is well reflected from the corresponding strain profiles (Fig. 7 b, c), marked by two outstanding peaks of nearly equal amplitudes in the low-amplitude spectrum. The peak density distribution indicates a large part of plastic strain partitioning selectively in the flaw-controlled conjugate bands. As the model deformation progresses, the circular flaw is deformed into an elliptical shape, and the model produces several secondary shear bands, although of much lower thickness in conjugate sets at $\varepsilon > 15\%$ (Fig. 6c-iii). This complex band structure is evident from multiple peaks in the strain profiles (Fig. 7c-iv), where the secondary peaks have amplitudes much lower than the principal peaks, implying that the flaw-controlled bands mainly accommodate the bulk strain, even after localization of the secondary bands. The calculated stress-strain curve (Fig. 5c) for MS3 indicates that the heterogeneous model attains the state of complete failure much earlier than MS1.

4. Geological relevance

4.1. Field study approach

Both the laboratory experiments and FE model simulations suggest that pre-existing mechanical flaws are necessary agents to form isolated shear band/zones, as commonly encountered in most of the geological terrains. A flaw-free, homogeneous rock at the yield stress would produce numerous, spatially distributed narrow shear bands (cf. narrow bands observed in homogeneous PS experiments), but not isolated wide shear zones in host rocks. However, it is difficult to recognize the nucleation of a shear zone in relation to pre-existing flaws in the field because the length scale of shear zones eventually far exceeds the flaw dimension, leaving the flaws geometrically almost unrecognizable objects, as seen in the numerical simulations (Fig. 6). But, some of their characteristic features can reflect their flaw-controlled origin. We discuss here outcrop scale shear zones from the Chotonagpur Granite Gneissic Complex (CGGC) in the light of our heterogeneous model experiments. We chose three locations in the CGGC: 1) Bero Hillocks (23°32'09.5" N, 86°40'01.3" E) near Raghunathpur town, 2) outcrops on the Purulia-Asansol Road transect near Baraseni (23°25'20.9"N 86°28'48.8"E), and 3) Jasidih (24° 31′ 19.2″ N, 86° 38′ 51.72″ E) (Supplementary S8). The CGGC terrain consists of a variety of country rocks, such as porphyritic granite gneisses, khondalite, amphibolite and mafic granulite. Our field studies concentrated in mylonitized shear zones within banded and augen granite gneisses. An elaborate description of the CGGC is provided in Supplementary S8.

4.2. Field observations and their analysis

Three distinct types of shear zones were recognized based on their internal shear structures and the nature of contact with the relatively less deformed host rock: Type I – isolated, narrow shear zones with maximum shear focused in the central zone, forming sharp boundaries with the unsheared walls (Fig. 8a), Type II – broad shear zones, consisting of a sheared core, defined by a cluster of narrow shear bands, where the entire composite structure is bounded by a drag zone on its either side (Fig. 8b), and Type III - thick homogeneous shear zones with a narrow diffused zone, forming a gradational boundary with the unsheared host (Fig. 8 c). As these contrasting types occur in the same rocks, the lithology does not seem to be a prime factor in controlling the varying modes of band formation in our study area.

Type I shear structures, observed in an outcrop of garnet-bearing quartzo-feldspathic gneissic rocks (location 2) near Purulia town, characteristically show intense shear localization (ε > 12) in narrow (thickness: ~2mm - ~5cm), linear zones, with their strike length on a few centimeters (Fig. 8a). High-resolution structural mapping {scale 1:100} (Fig. 9a-i) reveals that they are spatially distributed over the entire outcrop, and their statistical orientations define a conjugate set (Fig. 9a-ii) with a dihedral angle of ~70°-75° (Fig 9a-iii). In overall, this type of shear zones resembles narrow shear bands produced in homogeneous polystyrene models (Fig. 2a) and numerical simulations (Fig. 6a) that typically show an abrupt transition of shear strain across them (Fig. 9b-i), without showing any significant drag zone. In many places of our study area, such as Raghunathpur - Bero Hills (Location 1) and Jasidih (Location 3) we observed Type II shear zones in mylonitic granite gneissic hosts. This type of shear zone structures often localizes against quartzo-feldshapthic lenses in conjugate sets (Fig. 8b), as in the heterogeneous PS model experiments under high compression rates (Fig. 2b). The bands contain a strongly sheared core (~20 – 50 cm), flanked by wide transition zones (~5-10 cm to ~1-2 m) that gradually reduce shear strain from the core to unsheared walls. Although the shear zones are devoid of orthogonal narrow bands on macro-scales, they form typically a core - drag zone complex structure, which is comparable to composite bands produced in the heterogeneous models at high shear rates (Fig. 2b). Type III shear zones contain a thick, homogeneously sheared core (~15-20cm), bordered by a narrow zone of gradational shear on either side of the core (Fig. 8c). They look like flaw-controlled homogeneous bands in the polysterene experiments under relatively slow rates. Both Type II and III shear zones had long strike lengths, ranging from a fraction to tens of meters, irrespective of their core thickness. Type II strain profiles reveal gradational shear strain variation from the unsheared wall to core, forming a bell like pattern (Fig. 9 b-ii, Details in Supplementary S9). In contrast, Type III is characterized by a plateau-like structure of their strain profiles (Fig. 9b-iii).

5. Discussions

5.1. Physical factors controlling the band growth patterns

Earlier studies demonstrated the evolution of micro-bands (cf. narrow bands) from plane-strain compression experiments on various solids, such as steels and polymers (Anand & Spitzig, 1982; Bowden & Raha, 1970). The micro-bands generally multiply their number with increasing compressional strain, hardly showing any growth in thickness. Bowden and Raha's (1970) elaborate experiments with PMMA and PS show a transition from micro- to diffuse shear band formation as a function of temperature and strain rate. For example, their experiments find the micro-band mechanism as the dominant mechanism of plastic strain localization in polystyrene at room temperature (21°C), completely replaced by diffuse shear bands at higher temperatures (60°C to 70°C). They showed the same transition by lowering the strain-rate of the test from 2.3 x 10^{-2} s^{-1} to 6.0 x10^{-3} s^{-1}. These experimental results can be used to predict the band transition conditions, in terms of thermal or kinematic conditions, but it is applicable for mechanically homogeneous materials. Rocks and natural materials, such as soils are, however, heterogeneous due to various geological reasons (discussed later), and their heterogeneities can largely influence the process of shear-band formation in them (Grujic & Mancktelow, 1998; Pennacchioni & Mancktelow, 2007). We thus include pre-existing heterogeneities as an additional factor in this study, with an aim to widen the applicability of the previous experimental findings for inherently heterogeneous material systems. Our laboratory experiments suggest that the presence of mechanical flaws can result in a transition of the shear band mechanism under the same temperature and bulk strain conditions. For example, homogeneous PS models produce spatially distributed narrow shear bands (cf. micro-bands of Bowden and Raha) with a dihedral angle ~85° at room temperature condition and a strain rate of 3×10^{-5} s^{-1} (Fig. 3a). The same experimental condition produces band formation in a localized mode, forming a composite band structure when the material contains a tiny circular flaw. The composite shear bands form in conjugate sets with a dihedral angle of ~86°-90°. It follows from this discussion that the transition from distributed to localized band formation may not always reflect a drop in strain rate or lowering in temperature, as interpreted in earlier studies (Bowden & Raha, 1970). This can occur in the same location under the same physical condition, depending on the availability of inherent mechanical heterogeneities, as observed in our study area discussed in the preceding section. Structural overprinting relations, e.g. shear localization and foliation of particular generations, suggest that they formed in the same phase of deformation. In addition, the temperature and the strain rate conditions are unlikely to change to a large extent in an outcrop or a small part of the study area. We suggest that varying shear band patterns observed in the CGGC might have originated from inherent mechanical heterogeneities in mylonitized gneissic granites.

5.2. Geological origin of mechanical heterogeneities

Geological terrains evolve through complex petrogenetic and tectonic processes that eventually result in heterogeneous characteristics of the rocks on a wide range of scales: micro-scale, such as mechanically contrasting mineral grains and grain scale fractures, to kilometer scales, such as magma bodies (plutons) and fault zones. This study deals with weak flaws in a continuum, as they represent the most common type of mechanical heterogeneities encountered in the rock systems. This discussion thus focuses upon the origin of mechanically weak flaws in crustal rocks. A group of such flaws originate from petrological processes, such as partial melting, hydrothermal fluid enrichment and localized hydrolytic weakening. Partial melting in high-grade metamorphic conditions (p = ~3-4 Kb and T = ~750°C – 900°C) produces isolated melt pockets on macroscopic scale (a few millimeters to several centimeters), as reported from many field studies (Dijkstra et al., 2002; Kelemen & Dick, 1995; Lee et al., 2018; Piazolo et al., 2020). Both theoretical and experimental estimates suggest that the viscosity of quartzo-feldspathic melts ranges 3.9×10^{-3} to 1×10^{-2} Pa s, depending upon the volume content of solid crystals in them (Holtz et al., 1999). Assuming the viscosity of mylonitic granite crust in the order of 10^{21} Pa s at the corresponding P-T condition (D. L. Kohlstedt, 2007), the viscosity ratio of melt pockets to their host is found to be extremely low (~0.22), implying that the melt pockets would mechanically act almost like holes in the bulk rocks, similar to the consideration in the polystyrene models. Interestingly, such weak zones can be effective agents to localize outcrop scale shear zones in metamorphic terrains. Hydrothermal alteration is another important weak-zone forming mechanism at shallow to mid-crustal depths (Adak et al., 2021; Kalczynski & Gates, 2014; Rolland et al., 2003). Such alteration generally produces a variety of phyllosilicates, depending upon the geochemical composition and temperature of the hydrothermal fluids. Experimental studies suggest that phyllosilicate enrichments can lower the viscosity by several orders (Misra, Burlini, et al., 2009), forming isolated weak mechanical heterogeneities, especially in crustal terrains that undergo intense fluid activities, as imprinted in abundant pegmatitic bodies.

Another group of weak heterogeneities originate from mechanical processes, such as crack development and fracturing of rocks. Tensile fractures, for example, often form with a finite length, and they subsequently open out, forming lenticular zones, filled with leucosome materials. Field studies have reported localization of conjugate shear zones against such leucosome pods (Grujic & Mancktelow, 1998) and nodal veins of boudinage structures, formed by tensile fractures. With continued deformations the opening fractures act as weak zones to cause stress concentrations (Misra, Mandal, et al., 2009). Such mechanical heterogeneities provide seeds for preferential plastic yielding to initiate shear bands in the bulk continua (Eshelby, 1959; Rutter et al., 1986), as also reported in several geological studies (Grujic & Mancktelow, 1998; Meyer et al., 2017; Misra & Mandal, 2007; Roy et al., 2021). These seed heterogeneities formed by melt weakening, hydrous phase weakening or mechanical weakening generally have strength ratios in the order of 10^{-7} with the surrounding host rocks (Hack & Thompson, 2011). As a result, these pockets effectively act as voids in terms of their mechanical strength. We chose epoxy of extremely low yield strength (~7 MPa) to replicate such weak zones in our models, and maintained normal stresses at the matrix-weak zone interface, a condition that prevails in natural settings. It is noteworthy that the weak zone walls would crack in the absence of any filling material in the model as they become free from normal stresses.

5.3. Macroscopic rheology in shear zone modelling

To model purely viscous or visco-plastic shear zones in rocks, the crucial step demands an appropriate rheological framework with a close approximation to the geological conditions of interest (Bercovici & Karato, 2002; Gerya & Yuen, 2007; Popov & Sobolev, 2008). Previous works have used a wide spectrum of rheologies in shear zone modelling, ranging from power-law viscous (Fleitout & Froidevaux, 1980; Yuen et al., 1978; Yuen & Schubert, 1977) to complex visco-elasto-plastic rheology (Babeyko & Sobolev, 2008; Gerya & Yuen, 2007; Kaus, 2010). However, visco-plastic and elasto-plastic rheologies are perhaps the most commonly used rheological classes (Duretz et al., 2019; Roy et al., 2022). Both of them have certain drawbacks for ductile shear zone modeling. On one hand, the non-associative plasticity for visco-plastic media applies to weak and narrow brittle fault zones that can hardly represent the entire lithosphere. Furthermore, modelling based on this rheological consideration produces transient shear bands that fail to grow steadily to attain a mature state as they are immediately replaced by new generation of bands in the course of progressive deformation (Regenauer-Lieb & Yuen, 2003). The other drawback concerns the exaggeration of brittle responses in the model over the ductile contribution that critically determines the growth of shear zones in ductile or brittle-ductile regimes, as applicable to lithospheric deformations. To overcome these shortcomings, we use an elasto-visco-plastic rheology to model ductile shear zones around a weak zone. This rheological approximation simulates them in agreement with the field observations reported earlier (Grujic & Mancktelow, 1998; Meyer et al., 2017; Misra & Mandal, 2007) and in this study.

5.4. Limitations

This study is entirely based on laboratory experiments run at room temperature, and excludes the possible effects of temperature on shear band growth, as the main aim targets at understanding how a mechanical heterogeneity can independently mediate the mechanism of shear band localization in a rock under compression. Previous studies e.g., Bowden & Raha, (1970) have demonstrated from experiments that the temperature can largely influence the shear band pattern. Further experimental investigations, combining the effects of temperature and mechanical flaws, can provide a better approximation to actual geological conditions. Secondly, both the laboratory experiments and numerical modelling accounts for pure shear to represent the bulk deformations. Field studies reported shear zone development in complex tectonic settings, such as transpression where simple shear acts a major component in the bulk rock deformations. This study is applicable to geological terrains where mechanical heterogeneities occur in low concentrations without showing their mutual interactions. Here the effects of interacting heterogeneities in higher concentration (Ioannidi et al., 2021; Mandal et al., 2004) has not been studied. Many rocks develop tectonic fabrics, such as foliation either prior or during the event of shear zone formation. Such fabrics can introduce mechanical anisotropy in the bulk rocks. Our study does not explore the possible role of such anisotropy in the shear band growth around weak zones, which is a limitation and opens a scope for further investigation.

6. Conclusions

1) Analogue laboratory experiments confirm earlier geological observations that inherent mechanical heterogeneities in rocks act as potential nucleating seeds for shear zone formation. At a threshold stress rocks and similar solids without any inherent heterogeneities would always produce spatially distributed numerous narrow, sharp bands in conjugate sets with a dihedral angle of ~75°-85° to the compression direction. Their overall pattern is unlike isolated or solitary wide shear zones commonly observed in tectonic belts.

2) In homogeneous solids narrow bands begin to form at ~5% finite strain and multiply in number to increase their spatial density with increasing finite strain, and at the same time they grow in length with nearly a constant thickness.

3) The presence of weak heterogeneities results in a transition of spatially distributed narrow bands to isolated wide composite shear bands. The composite bands radiate from the circular

flaw in conjugate pairs with a dihedral angle of ~85°-90°. A typical composite shear band develops a characteristic internal band structures, consisting of a strongly sheared core (cluster of extremely close spaced sub-parallel narrow bands, flanked by a region of orthogonal similar bands on either side of it. The composite bands core accommodates most of the plastic strain in the band, leaving its flank regions for weak shear localization.

4) The mechanism of heterogeneity-controlled shear band localization is sensitive to the global strain rate ($\dot{\varepsilon}$). Reducing $\dot{\varepsilon}$ replaces composites bands with wide, homogeneous shear bands, which are completely devoid of narrow bands.

5) The real scale (both space and time) 2D finite element models, based on visco-elasto plastic rheology validate the following laboratory findings: i) transition in the mechanism of band formation (spatially distributed narrow bands to localized composite bands) depending on the absence or presence of an inherent weak flaw, and ii) Composite to homogenous shear band transformation with reducing global strain rates.

6) Heterogeneous mechanical models explain the diverse types of shear zones commonly observed in many geological terrains, like CGGC.

Acknowledgements

We thank Prof. Laetita Le Pourhiet, an anonymous reviewer and the Associate Editor for their incisive comments and constructive reviews, which significantly helped in improving this manuscript. We also thank Editor Prof. Douglas Schmitt for his insightful guideline in revising the manuscript. The present work has been supported by the SERB-DST, Government of India, with J. C. Bose Fellowship (SR/S2/JCB-36/ 2012) to N. M. and by the BRNS with a research project (36(2)/14/25/2016- BRNS). CSIR, India is gratefully acknowledged for awarding research fellowship grants to A.R. (09/096(0940)/2018-EMR-I). M.M. acknowledges BRNS for awarding fellowship grant under research project (36(2)/14/25/2016- BRNS).

Data Availability Statement

The relevant data supporting the conclusions are present in this manuscript and in the supplementary information. All aspects of UNDERWORLD 2 can be downloaded and checked here (https://www.underworldcode.org/).

References

Adak, S., Pal, D. C., Upadhyay, D., & Mondal, R. (2021). Textural re-equilibration, hydrothermal alteration and element redistribution in Fe-Ti oxide pods, Singhbhum Shear Zone, eastern India. *Geochemistry*, *81*(1), 125679. https://doi.org/10.1016/j.chemer.2020.125679

Anand, L., & Spitzig, W. A. (1980). Initiation of localized shear bands in plane strain. *Journal of the Mechanics and Physics of Solids*, *28*(2), 113–128. https://doi.org/10.1016/0022-5096(80)90017-4

Anand, L., & Spitzig, W. A. (1982). Shear-Band Orientations in Plane Strain. *Acta Metallurgica*, *30*(2), 553–561.

Babeyko, A. Y., & Sobolev, S. V. (2008). High-resolution numerical modeling of stress distribution in visco-elasto-plastic subducting slabs. *Lithos*, *103*(1–2), 205–216. https://doi.org/10.1016/j.lithos.2007.09.015

Beall, A., Fagereng, Å., & Ellis, S. (2019). Fracture and Weakening of Jammed Subduction Shear Zones, Leading to the Generation of Slow Slip Events. *Geochemistry, Geophysics, Geosystems*, *20*(11), 4869–4884. https://doi.org/10.1029/2019GC008481

Bercovici, D., & Karato, S. I. (2002). Theoretical analysis of shear localization in the lithosphere. *Reviews in Mineralogy and Geochemistry*. https://doi.org/10.2138/gsrmg.51.1.387

Bowden, P. B., & Raha, S. (1970). The formation of micro shear bands in polystyrene and polymethylmethacrylate. *Philosophical Magazine*, *22*(177), 463–482. https://doi.org/10.1080/14786437008225837

Camwell, L., & Hull, D. (1973). Crazing and fracture associated with the interaction of shear bands in polystyrene. *Philosophical Magazine*, *27*(5), 1135–1150. https://doi.org/10.1080/14786437308225822

Carreras, J., Czeck, D. M., Druguet, E., & Hudleston, P. J. (2010). Structure and development of an anastomosing network of ductile shear zones. *Journal of Structural Geology*, *32*(5), 656–666. https://doi.org/10.1016/j.jsg.2010.03.013

Dijkstra, A. H., Drury, M. R., & Frijhoff, R. M. (2002). Microstructures and lattice fabrics in the

Hilti mantle section (Oman Ophiolite): Evidence for shear localization and melt weakening in the crust-mantle transition zone? *Journal of Geophysical Research: Solid Earth*, *107*(B11), ETG 2-1-ETG 2-18. https://doi.org/10.1029/2001jb000458

Drucker, D. C., & Prager, W. (1952). Soil mechanics and plastic analysis or limit design. *Quarterly of Applied Mathematics*, *10*(2), 157–165.

Duretz, T., de Borst, R., & Le Pourhiet, L. (2019). Finite Thickness of Shear Bands in Frictional Viscoplasticity and Implications for Lithosphere Dynamics. *Geochemistry, Geophysics, Geosystems*, *20*(11), 5598–5616. https://doi.org/10.1029/2019GC008531

Eshelby, J. D. (1959). The elastic field outside an ellipsoidal inclusion. *Proceedings of the Royal Society of London. Series A. Mathematical and Physical Sciences*, *252*(1271), 561–569. https://doi.org/10.1098/rspa.1959.0173

Farrington, R. J., Moresi, L. N., & Capitanio, F. A. (2014). The role of viscoelasticity in subducting plates. *Geochemistry, Geophysics, Geosystems*, *15*(11), 4291–4304. https://doi.org/10.1002/2014GC005507.Received

Finch, M. A., Bons, P. D., Steinbach, F., Griera, A., Llorens, M. G., Gomez-Rivas, E., et al. (2020). The ephemeral development of C′ shear bands: A numerical modelling approach. *Journal of Structural Geology*, *139*(December 2019), 104091. https://doi.org/10.1016/j.jsg.2020.104091

Finch, M. A., Bons, P. D., Weinberg, R. F., Llorens, M. G., Griera, A., & Gomez-Rivas, E. (2022). A dynamic atlas of interference patterns in superimposed, opposite sense ductile shear zones. *Journal of Structural Geology*, *165*(October), 104739. https://doi.org/10.1016/j.jsg.2022.104739

Fleitout, L., & Froidevaux, C. (1980). Thermal and mechanical evolution of shear zones. *Journal of Structural Geology*, *2*(1–2), 159–164. https://doi.org/10.1016/0191-8141(80)90046-2

Fossen, H., Schultz, R. A., Shipton, Z. K., & Mair, K. (2007). Deformation bands in sandstone: A review. *Journal of the Geological Society*, *164*(4), 755–769. https://doi.org/10.1144/0016-76492006-036

Fusseis, F., & Handy, M. R. (2008). Micromechanisms of shear zone propagation at the brittle-viscous transition. *Journal of Structural Geology*, *30*(10), 1242–1253. https://doi.org/10.1016/j.jsg.2008.06.005

Fusseis, F., Handy, M. R., & Schrank, C. (2006). Networking of shear zones at the brittle-to-viscous transition (Cap de Creus, NE Spain). *Journal of Structural Geology*, *28*(7), 1228–1243. https://doi.org/10.1016/j.jsg.2006.03.022

Gapais, D. (1989). Shear structures within deformed granites: mechanical and thermal indicators. *Geology*, *17*(12), 1144–1147. https://doi.org/10.1130/0091-7613(1989)017<1144:SSWDGM>2.3.CO;2

Gerya, T. V., & Yuen, D. A. (2007). Robust characteristics method for modelling multiphase visco-elasto-plastic thermo-mechanical problems. *Physics of the Earth and Planetary Interiors*, *163*(1–4), 83–105. https://doi.org/10.1016/j.pepi.2007.04.015

Ghosh, S. K., & Sengupta, S. (1987). Progressive development of structures in a ductile shear zone. *Journal of Structural Geology*, *9*(3), 277–287. https://doi.org/https://doi.org/10.1016/0191-8141(87)90052-6

Grujic, D., & Mancktelow, N. S. (1998). Melt-bearing shear zones: analogue experiments and comparison with examples from southern Madagascar. *Journal of Structural Geology*, *20*(6), 673–680. https://doi.org/10.1016/S0191-8141(98)00006-6

Hack, A. C., & Thompson, A. B. (2011). Density and viscosity of hydrous magmas and related fluids and their role in subduction zone processes. *Journal of Petrology*, *52*(7–8), 1333–1362. https://doi.org/10.1093/petrology/egq048

Holtz, F., Roux, J., Ohlhorst, S., Behrens, H., & Schulze, F. (1999). The effects of silica and water on the viscosity of hydrous quartzofeldspathic melts. *American Mineralogist*, *84*(1–2), 27–36. https://doi.org/10.2138/am-1999-1-203

Holtzman, B. K., Kohlstedt, D. L., Zimmerman, M. E., Heidelbach, F., Hiraga, T., & Hustoft, J. (2003). Melt segregation and strain partitioning: Implications for seismic anisotropy and mantle flow. *Science*, *301*(5637), 1227–1230. https://doi.org/10.1126/science.1087132

Holtzman, B. K., Groebner, N. J., Zimmerman, M. E., Ginsberg, S. B., & Kohlstedt, D. L. (2003). Stress-driven melt segregation in partially molten rocks. *Geochemistry, Geophysics, Geosystems*, *4*(5). https://doi.org/10.1029/2001GC000258

Ioannidi, P. I., Le Pourhiet, L., Agard, P., Angiboust, S., & Oncken, O. (2021). Effective rheology of a two-phase subduction shear zone: Insights from numerical simple shear experiments and implications for subduction zone interfaces. *Earth and Planetary Science Letters*, *566*, 116913. https://doi.org/10.1016/j.epsl.2021.116913

Kalczynski, M. J., & Gates, A. E. (2014). Hydrothermal alteration, mass transfer and magnetite mineralization in dextral shear zones, western Hudson Highlands, New York, United States. *Ore Geology Reviews*, *61*, 226–247. https://doi.org/10.1016/j.oregeorev.2014.02.007

Katz, Y., Weinberger, R., & Aydin, A. (2004). Geometry and kinematic evolution of Riedel shear structures, Capitol Reef National Park, Utah. *Journal of Structural Geology*, *26*(3), 491–501. https://doi.org/10.1016/j.jsg.2003.08.003

Kaus, B. J. P. (2010). Factors that control the angle of shear bands in geodynamic numerical models of brittle deformation. *Tectonophysics*, *484*(1–4), 36–47. https://doi.org/10.1016/j.tecto.2009.08.042

Kelemen, P. B., & Dick, H. J. B. (1995). Focused melt flow and localized deformation in the upper mantle: juxtaposition of replacive dunite and ductile shear zones in the Josephine peridotite, SW Oregon. *Journal of Geophysical Research*, *100*(B1), 423–438. https://doi.org/10.1029/94JB02063

Kohlstedt, D. L. (2007). Properties of Rocks and Minerals - Constitutive Equations, Rheological Behavior, and Viscosity of Rocks. *Treatise on Geophysics*, *2*, 389–417. https://doi.org/10.1016/B978-044452748-6.00043-2

Kohlstedt, David L., & Holtzman, B. K. (2009). Shearing melt out of the earth: An experimentalist's perspective on the influence of deformation on melt extraction. *Annual Review of Earth and Planetary Sciences*, *37*, 561–593. https://doi.org/10.1146/annurev.earth.031208.100104

Lee, A. L., Torvela, T., Lloyd, G. E., & Walker, A. M. (2018). Melt organisation and strain partitioning in the lower crust. *Journal of Structural Geology*. https://doi.org/10.1016/j.jsg.2018.05.016

Lemiale, V., Mühlhaus, H. B., Moresi, L., & Stafford, J. (2008). Shear banding analysis of plastic models formulated for incompressible viscous flows. *Physics of the Earth and Planetary Interiors*, *171*(1–4), 177–186. https://doi.org/10.1016/j.pepi.2008.07.038

Mancktelow, N. S., & Pennacchioni, G. (2005). The control of precursor brittle fracture and fluid-rock interaction on the development of single and paired ductile shear zones. *Journal of Structural Geology*, *27*(4), 645–661. https://doi.org/10.1016/j.jsg.2004.12.001

Mandal, N., Misra, S., & Samanta, S. K. (2004). Role of weak flaws in nucleation of shear zones: An experimental and theoretical study. *Journal of Structural Geology*, *26*(8), 1391–1400. https://doi.org/10.1016/j.jsg.2004.01.001

Mansour, J., Giordani, J., Moresi, L., Beucher, R., Kaluza, O., Velic, M., et al. (2020). Underworld2: Python geodynamics modelling for desktop, HPC and cloud. *Journal of Open Source Software*, *5*(47). https://doi.org/10.1130/G39943.1

Mauldon, M., Dunne, W. M., & Rohrbaugh, M. B. (2001). Circular scanlines and circular windows: New tools for characterizing the geometry of fracture traces. *Journal of Structural Geology*, *23*(2–3), 247–258. https://doi.org/10.1016/S0191-8141(00)00094-8

Meyer, S. E., Kaus, B. J. P., & Passchier, C. (2017). Development of branching brittle and ductile shear zones: A numerical study. *Geochemistry, Geophysics, Geosystems*, *18*, 2054–2075. https://doi.org/10.1002/2016GC006793.Received

Misra, S., & Mandal, N. (2007). Localization of plastic zones in rocks around rigid inclusions: Insights from experimental and theoretical models. *Journal of Geophysical Research: Solid Earth*, *112*(9), 1–15. https://doi.org/10.1029/2006JB004328

Misra, S., Mandal, N., & Chakraborty, C. (2009). Formation of Riedel shear fractures in granular materials: Findings from analogue shear experiments and theoretical analyses. *Tectonophysics*, *471*(3–4), 253–259. https://doi.org/10.1016/j.tecto.2009.02.017

Misra, S., Burlini, L., & Burg, J. P. (2009). Strain localization and melt segregation in deforming metapelites. *Physics of the Earth and Planetary Interiors*, *177*(3–4), 173–179. https://doi.org/10.1016/j.pepi.2009.08.011

Moresi, L., Dufour, F., & Muhlhaus, H. B. (2003). A Lagrangian integration point finite element method for large deformation modeling of viscoelastic geomaterials. *Journal of Computational Physics*, *184*(2), 476–497. https://doi.org/10.1016/S0021-9991(02)00031-1

Moresi, L., Quenette, S., Lemiale, V., Mériaux, C., Appelbe, B., & Mühlhaus, H. B. (2007). Computational approaches to studying non-linear dynamics of the crust and mantle. *Physics of the Earth and Planetary Interiors*, *163*(1–4), 69–82. https://doi.org/10.1016/j.pepi.2007.06.009

Nizolek, T. J., Pollock, T. M., & McMeeking, R. M. (2021). Kink band and shear band localization in anisotropic perfectly plastic solids. *Journal of the Mechanics and Physics of Solids*, *146*(July 2019), 104183. https://doi.org/10.1016/j.jmps.2020.104183

Pennacchioni, G., & Mancktelow, N. S. (2018). Small-scale ductile shear zones: Neither extending, nor thickening, nor narrowing. *Earth-Science Reviews*, *184*(June), 1–12. https://doi.org/10.1016/j.earscirev.2018.06.004

Pennacchioni, Giorgio, & Mancktelow, N. S. (2007). Nucleation and initial growth of a shear zone network within compositionally and structurally heterogeneous granitoids under amphibolite facies conditions. *Journal of Structural Geology*, *29*(11), 1757–1780. https://doi.org/10.1016/j.jsg.2007.06.002

Piazolo, S., Daczko, N. R., Silva, D., & Raimondo, T. (2020). Melt-present shear zones enable intracontinental orogenesis. *Geology*. https://doi.org/10.1130/G47126.1

Popov, A. A., & Sobolev, S. V. (2008). SLIM3D: A tool for three-dimensional thermomechanical modeling of lithospheric deformation with elasto-visco-plastic rheology. *Physics of the Earth and Planetary Interiors*, *171*(1–4), 55–75. https://doi.org/10.1016/j.pepi.2008.03.007

Reber, J. E., Cooke, M. L., & Dooley, T. P. (2020). What model material to use? A Review on rock analogs for structural geology and tectonics. *Earth-Science Reviews*, *202*(September 2019), 103107. https://doi.org/10.1016/j.earscirev.2020.103107

Regenauer-Lieb, K., & Yuen, D. A. (2003). Modeling shear zones in geological and planetary sciences: Solid- and fluid-thermal-mechanical approaches. *Earth-Science Reviews*, *63*(3–4), 295–349. https://doi.org/10.1016/S0012-8252(03)00038-2

Rogowitz, A., White, J. C., & Grasemann, B. (2016). Strain localization in ultramylonitic marbles by simultaneous activation of dislocation motion and grain boundary sliding (Syros, Greece). *Solid Earth*, *7*(2), 355–366. https://doi.org/10.5194/se-7-355-2016

Rolland, Y., Cox, S., Boullier, A. M., Pennacchioni, G., & Mancktelow, N. (2003). Rare earth and trace element mobility in mid-crustal shear zones: Insights from the Mont Blanc Massif (Western Alps). *Earth and Planetary Science Letters*, *214*(1–2), 203–219. https://doi.org/10.1016/S0012-821X(03)00372-8

Roy, A., Roy, N., Saha, P., & Mandal, N. (2021). Factors Determining Shear-Parallel Versus Low-Angle Shear Band Localization in Shear Deformations: Laboratory Experiments and Numerical Simulations. *Journal of Geophysical Research: Solid Earth*, *126*(10), 1–23. https://doi.org/10.1029/2021JB022578

Roy, A., Saha, P., & Mandal, N. (2022). Viscoplastic Rheological Modelling- A Realistic Approach to Natural Ductile Shear Zones, (April), 2022.

Roy, N., Roy, A., Saha, P., & Mandal, N. (2022). On the origin of shear-band network patterns in ductile shear zones. *Proceedings of the Royal Society A: Mathematical, Physical and Engineering Sciences*, *478*(2264). https://doi.org/10.1098/rspa.2022.0146

Rutter, E. H., Maddock, R. H., Hall, S. H., & White, S. H. (1986). Comparative microstructures of natural and experimentally produced clay-bearing fault gouges. *Pure and Applied Geophysics PAGEOPH*, *124*(1–2), 3–30. https://doi.org/10.1007/BF00875717

Sagapuram, D., Viswanathan, K., Trumble, K. P., & Chandrasekar, S. (2018). A common mechanism for evolution of single shear bands in large-strain deformation of metals. *Philosophical Magazine*, *98*(36), 3267–3299. https://doi.org/10.1080/14786435.2018.1524586

Scholz, C. H., & Choi, E. (2021). What comes first: The fault or the ductile shear zone? *Earth and Planetary Science Letters*, *577*, 117273. https://doi.org/10.1016/j.epsl.2021.117273

Snell, T., De Paola, N., van Hunen, J., Nielsen, S., & Collettini, C. (2020). Modelling fluid flow in complex natural fault zones: Implications for natural and human-induced earthquake nucleation. *Earth and Planetary Science Letters*, *530*, 115869.

https://doi.org/10.1016/j.epsl.2019.115869

Snyder, D. B., & Kjarsgaard, B. A. (2013). Mantle roots of major precambrian shear zones inferred from structure of the great slave lake shear zone, northwest Canada. *Lithosphere*, *5*(6), 539–546. https://doi.org/10.1130/L299.1

Vauchez, A., Tommasi, A., & Mainprice, D. (2012). Faults (shear zones) in the Earth's mantle. *Tectonophysics*, *558–559*, 1–27. https://doi.org/10.1016/j.tecto.2012.06.006

Willis, K., Houseman, G. A., Evans, L., Wright, T., & Hooper, A. (2019). Strain localization by shear heating and the development of lithospheric shear zones. *Tectonophysics*, *764*(December 2018), 62–76. https://doi.org/10.1016/j.tecto.2019.05.010

Yuen, D. A., Fleitout, L., Schubert, G., & Froidevaux, C. (1978). Shear deformation zones along major transform faults and subducting slabs. *Geophysical Journal of the Royal Astronomical Society*, *54*(1), 93–119. https://doi.org/10.1111/j.1365-246X.1978.tb06758.x

Yuen, David A., & Schubert, G. (1977). ASTHENOSPHERIC SHEAR FLOW: THERMALLY STABLE OR UNSTABLE? *Geophysical Research Letters*, *4*(11).

Zielinski, P. G., & Ast, D. G. (1983). Slip bands in metallic glasses. *Philosophical Magazine A: Physics of Condensed Matter, Structure, Defects and Mechanical Properties*, *48*(5), 811–824. https://doi.org/10.1080/01418618308236546

Appendix A:

Governing equations, numerical parameters and their constitutive relationships

To describe the model rheology, we consider the first and second invariants of stress tensor (σ_{ij}):

$$I_1 = \sigma_{jj}\,; \qquad (1)$$

$$I_2 = \frac{\sigma_{ii}\sigma_{jj} - \sigma_{ij}\sigma_{ij}}{2} \qquad (2)$$

Decomposing σ_{ij} into the isotropic (${\sigma^o}_{ij}$) and the deviatoric stress (${\sigma^s}_{ij}$) tensors, it follows

$${\sigma^o}_{ij} = \frac{1}{3}\sigma_{kk}\delta_{ij} \text{ and } {\sigma^s}_{ij} = \sigma_{ij} - {\sigma^o}_{ij}, \qquad (3)$$

where δ_{ij} is Kronecker delta. From Eq. (2) and (3), the second stress invariant, I_2 is expressed as

$$I_2 = 3{{\sigma^o}_{jj}}^2 - \frac{1}{2}\sigma_{ij}\sigma_{ij} \qquad (4)$$

Assuming the material as incompressible, we obtain the total strain-rate tensor as a sum of elastic ($\dot{\varepsilon}^{e}_{ij}$), plastic ($\dot{\varepsilon}^{p}_{ij}$) and viscous ($\dot{\varepsilon}^{v}_{ij}$) strain-rates:

$$\dot{\varepsilon_{ij}} = \dot{\varepsilon}^{v}_{ij} + \dot{\varepsilon}^{p}_{ij} + \dot{\varepsilon}^{e}_{ij}, \qquad (5)$$

where $\dot{\varepsilon}^{v}_{ij} = \frac{1}{2}\frac{{\sigma^{s}}_{ij}}{\eta_v}$,

$$\dot{\varepsilon}^{p}_{ij} = \begin{cases} 0, & I_2 < \sigma_{yield} \\ \chi\left(\frac{1}{2}\frac{{\sigma^{s}}_{ij}}{I_2}\right), & I_2 \geq \sigma_{yield} \end{cases},$$

$$\dot{\varepsilon}^{e}_{ij} = \frac{1}{2G}\frac{D{\sigma^{s}}_{ij}}{Dt}$$

σ_{yield} denotes the yield strength of the material, *G* is the elastic shear module, η_v is the bulk viscosity of the material, and χ is a plastic multiplier, satisfying the yield condition, $I_2 = \sigma_{yeild}$.

Visco-elasticity in *UNDERWORLD2* is implemented by modifying the momentum equation using an effective viscosity and additional force term dependent on material properties, time step size and stress history (Moresi et al., 2003). A consequence of this consideration is that the force term depends on the numerical time step. The time scale of model run time is set at values lower than the numeric time step, determined by the model rheological set up. The two time scales need to be decoupled to ensure the effects of the time scale of interest. Without this time-scale manipulation, the model results would be affected by the grid resolution chosen for the simulation. To overcome this problem, we introduce an observation time step Δt_e, independent to the numeric time step (Farrington et al., 2014).

For the onset of plastic creep in our model, we introduce post-yield viscous weakening of the material (strain softening rheology), where the modified viscosity decreases nonlinearly with increasing plastic strain. This synkinematic rheological transformation is implemented by expressing the effective current viscosity as a function of strain rate and the yield stress (σ_e),

$$\eta_{eff} = \frac{\sigma_e}{|\dot{\varepsilon}_{eff}|}, \tag{6}$$

and $$\dot{\varepsilon}_{eff} = 2\,\dot{\varepsilon}^{t+\Delta t_e} + \frac{1}{G\Delta t_e}{\sigma^{s}}_{ij}^{\ t} , \tag{7}$$

where the superscripts t and $t + \Delta t_e$ indicate values at the current and future timestep, respectively. Δt_e denotes the timestep that captures the relevant timescales of the modifications in elastic stresses. The yield behaviour is modelled by employing a pressure-dependent plasticity criterion (Drucker-Prager), as considered by earlier workers (Roy et al., 2021; Snell et al., 2020). Based on this criterion, a yield function, $\mathcal{F}$ can be defined in the following form (Drucker & Prager, 1952)

$$\mathcal{F} = \sigma_e - \sqrt{3}\sin\emptyset\, P - \sqrt{3}\, C\left(\gamma_{pl}\right)\cos\emptyset \tag{8}$$

where $P = -\frac{1}{3}I_1$, and $C\left(\gamma_{pl}\right)$ is the material cohesion, expressed as a function of plastic strain γ_{pl} , and $\emptyset$ is the angle of internal friction. The cohesion is assumed to weaken with increasing accumulated plastic strain:

$$C = C_i + \left(C_f - C_i\right)\min(1, \frac{\gamma_{pl}}{\gamma_o}), \tag{9}$$

where C_i is the initial cohesion and C_f is the final cohesion of the shear zone material. Also, $\gamma_{pl} = \int_0^t \dot{\varepsilon}_p\, dt$, indicates accumulated plastic strain in regions where the yield limit is reached and $\gamma_o = 0.1$ is taken as the reference strain. No syn-deformational healing of the cohesion is implemented in this model.

Figure captions:

Figure 1: a) Schematic presentation of the deformation zig used for compression tests under plane strain condition. The orientations of the principal stress axes are shown in the corresponding panel. b) A perspective view of heterogeneous PS model, containing two through-going cylindrical weak flaws with their axes perpendicular to the principal compression direction (σ_1-axis) and aligned along the direction of no strain (σ_2-axis). The PS block was allowed to extend in the horizontal direction (σ_3-axis) at right angle to the flaw axis. (c) Stress versus strain relations for homogeneous and heterogeneous PS models obtained from laboratory experiments at low (2 x 10^{-5} s^{-1}) and high (3 X 10^{-5} s^{-1}) strain rates.

Figure 2: Structural characteristics of the three types of shear bands in PS models (thin sections under cross polars). a) Uniformly distributed narrow bands (NB) in homogeneous PS deformed at high $\dot{\varepsilon}$ (3 x 10^{-5} s^{-1}). Note that the bands define conjugate orientations (white dotted lines) with dihedral angle (Φ) of ~85°-88°; b) Composite band in a PS block containing weak flaws deformed at high $\dot{\varepsilon}$ (3 x 10^{-5} s^{-1}). The band structure is composed of a core zone (cluster of finely spaced parallel narrow bands), bounded by transition zone (marked by green color), containing a dominant set of orthogonal narrow bands. The red lines show the accommodated viscous drag in the transition zone. The core zone generally forms at a low angle (~ 10°-15°) to the overall band trend. c) Homogeneous band (HB) in a PS block with weak flaws deformed at low $\dot{\varepsilon}$ (2 x 10^{-5} s^{-1}) Note that the band shows a wide core zone of homogeneous internal shear strain, and a narrow zone of gradational shear, as revealed from optical birefringence.

Figure 3: Shear band growth in polystyrene model experiments with increasing finite strain. a) Uniform development of closely spaced, conjugate narrow bands (NB) in homogenous PS models deformed at high strain rate ($\dot{\varepsilon} = 3 \text{ X } 10^{-5}\ s^{-1}$). Note at higher finite strain, shear zone forms at a high angle to the compression direction, marked by dotted red line. b) Formation of wide composite bands preferentially against the weak flaws in a heterogeneous PS model at a high strain rate. The composite structure consists of a core and a transition zone (TZ), dominated by band-parallel and orthogonal narrow bands. Φ is half of the dihedral angle formed by the composite bands. c) Formation of homogeneously sheared bands (HB), bordered by narrow

zones of gradational shear contacts with the weakly strained walls. The heterogeneous PS model was deformed at a low strain rate (2 x 10^{-5} s^{-1}). The photographs are obtained from thin sections of deformed PS blocks observed under cross polarized light.

Figure 4: Geometrical analysis of shear band structures in a) homogenous PS models and b) PS models containing cylindrical weak flaws : i) histogram, ii) rose diagrams of band orientations, and iii) band density map. Note that the band density plots show a clear transition of distributed narrow bands in homogenous model to localized composite bands in a PS model with weak flaws, where the band core regions have the highest band concentrations.

Figure 5: a) Initial finite element (FE) model setup used for numerical experiments. The circle (yellow) at the center represents a weak flow in the FE model domain. Arrows indicate the kinematic boundary conditions imposed at the model boundaries. b) 1D rheological representation of the FE modelling. This decomposition can be interpreted as Maxwell visco-elasto-plastic rheology, where plastic, viscous and elastic components are connected in series. σ_e, η_v, and G: plastic yield stress, material viscosity and shear modulus of the material, respectively. c) Stress versus strain relations obtained from progressive deformations of visco-elasto-plastic numerical models. Note that the model with an initial weak flaw yields at a lower stress than a homogenous model (free from any initial flaw).

Figure 6: Progressive development of shear bands in a) a homogeneous model and b) a heterogeneous model with an initial weak flaw, deformed at high strain rates (2 x 10^{-12} s^{-1}), and c) a similar heterogeneous model, but deformed under a relatively low strain rate (5 x 10^{-14} s^{-1}). The finite model shortening is indicated at the top of each panel. Note that the core zones (red regions) in bands produced in the heterogeneous model under high strain rates (b) form at an angle (~7°-10°) to the overall band trend, as in the laboratory models (Fig 3b-iii)

Figure 7: Across-band strain profiles in deformed numerical models (locations of the profile lines: AB, CD, and EF, shown in inset). The percentage of shortening is indicated at the top of each panel. The profiles reveal systematic variations of accumulated strain value, where the

peaks demarcate the locations of shear band localization in a homogeneous and a heterogeneous model simulation: MS1 and MS3.

Figure 8: Field photographs of outcrop-scale shear zones in the Chotanagpur Granite Gneissic Complex (CGGC), Eastern India showing a) Narrow shear Bands, b) Composite shear Bands and c) Homogenous shear Bands. a-i) Multiple narrow shear zones (NB) of conjugate orientations distributed in a single ~100 m x 50 m outcrop of homogeneous quartzo-feldspathic rocks. a-ii) A single narrow band (3mm thickness) in an outcrop of banded gneiss. b-i) Heterogeneity (quartzo-feldspathic aggregates) controlled localization of composite shear bands in conjugate sets, radiating from the heterogeneity. Each band shows a core of strongly sheared rocks, flanked by foliation drag zones. b-ii) A single composite band formed along an inherent heterogeneity with prominent drag zone and strongly sheared core. c-i) and ii) Shear zones containing a wide band of homogeneous shear strain (core), bordered by narrow zones of relatively weak shear, grading into unsheared wall rocks.

Figure 9: a-i) High-resolution structural map (1:100) of a homogeneous quartzo-feldspathic outcrop showing spatially distributed numerous narrow bands (marked by red color) in conjugate sets. a-ii) Corresponding histogram and (a-iii) rose diagram of the shear band orientations shown in the map. b) Construction of across-band strain profiles based on field measurements: i) Type I, ii) Type II and iii) Type III shear zones, where ε is the finite strain and x is the horizontal distance across the shear band.

Figure 1.

a
σ1
Upper Piston
Sample
no strain
σ3
Deformation Jig
σ1
(compression)
σ3
(extension)
σ2 (no strain)
b
σ1
σ3
σ1
(compression)
σ2
(no strain)
20 mm
20 mm
60 mm
Cylindrical Holes
35 mm
Polysterene Block
c
Bulk Stress (MPa)
Finite Strain
0
20
40
60
80
100
120
140
160
0
0.02
0.04
0.06
0.08
0.1
0.12
0.14
0.16
0.18
Homogenous High Strain Rate
Homogenous Low Strain Rate
Heterogenous High Strain Rate
Heterogenous Low Strain Rate

Figure 2.


a
NB
b
Weakly Deformed wall
Transition zone
θ = 15°
Core
c
Gradational
Zone
HB
Gradational
Zone
Weakly Deformed
wall

Figure 3.

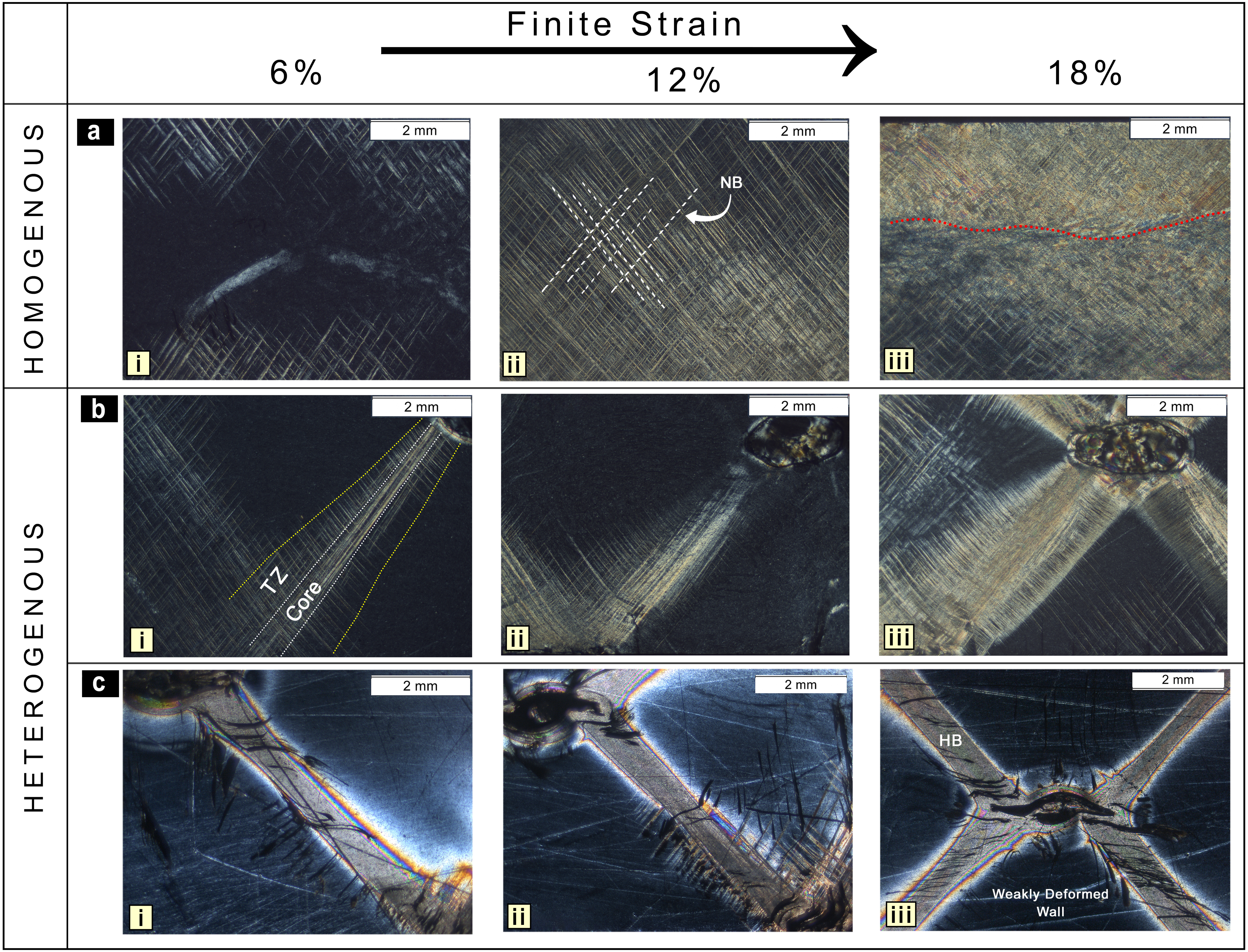
Finite Strain
6%
12%
18%
HOMOGENOUS
HETEROGENOUS
a
b
c
2 mm
NB
TZ
Core
HB
Weakly Deformed Wall
i
ii
iii

Figure 4.


HOMOGENOUS
Segment angles (equal area), n = 923
i
Frequency
Frequency, %
Trace Segment Angle, Degrees
ii
10%
5%
1%
iii
y (mm)
x (mm)
a
HETEROGENOUS
Segment angles , n = 1560
Segment angles (equal area), n = 1560
Heterogeneity
b

Figure 5.


a
V_l
Viscoelastoplastic Material
Imposed Heterogeneity
b
G
η_v
σ_e
c
Heterogenous Model (LSR)
Heterogenous Model (HSR)
Homogenous Model
16
12
8
4
σ (MPa)
0
0.5
1
1.5
2
ε (%)

Figure 6.

5%
10%
15%
20%
a
No Pre-existing Flaw
b
Pre-existing Flaw
c
Pre-existing Flaw (HSR)
i
ii
iii
iv
Accumulated Strain (ϵ_{II} x10^{-2})
4
2
0
8
4
0

Figure 7.

5%
10%
15%
20%
a
b
c
i
ii
iii
iv
A
B
C
D
E
F
0
0.1
0.2
0.3
0.4
0.6
0.8
1.0
Accumulated Strain (ϵ_{II} x 10^{-1})
Horizontal Distance
Heterogenous Model
Homogeneous Model

Figure 8.

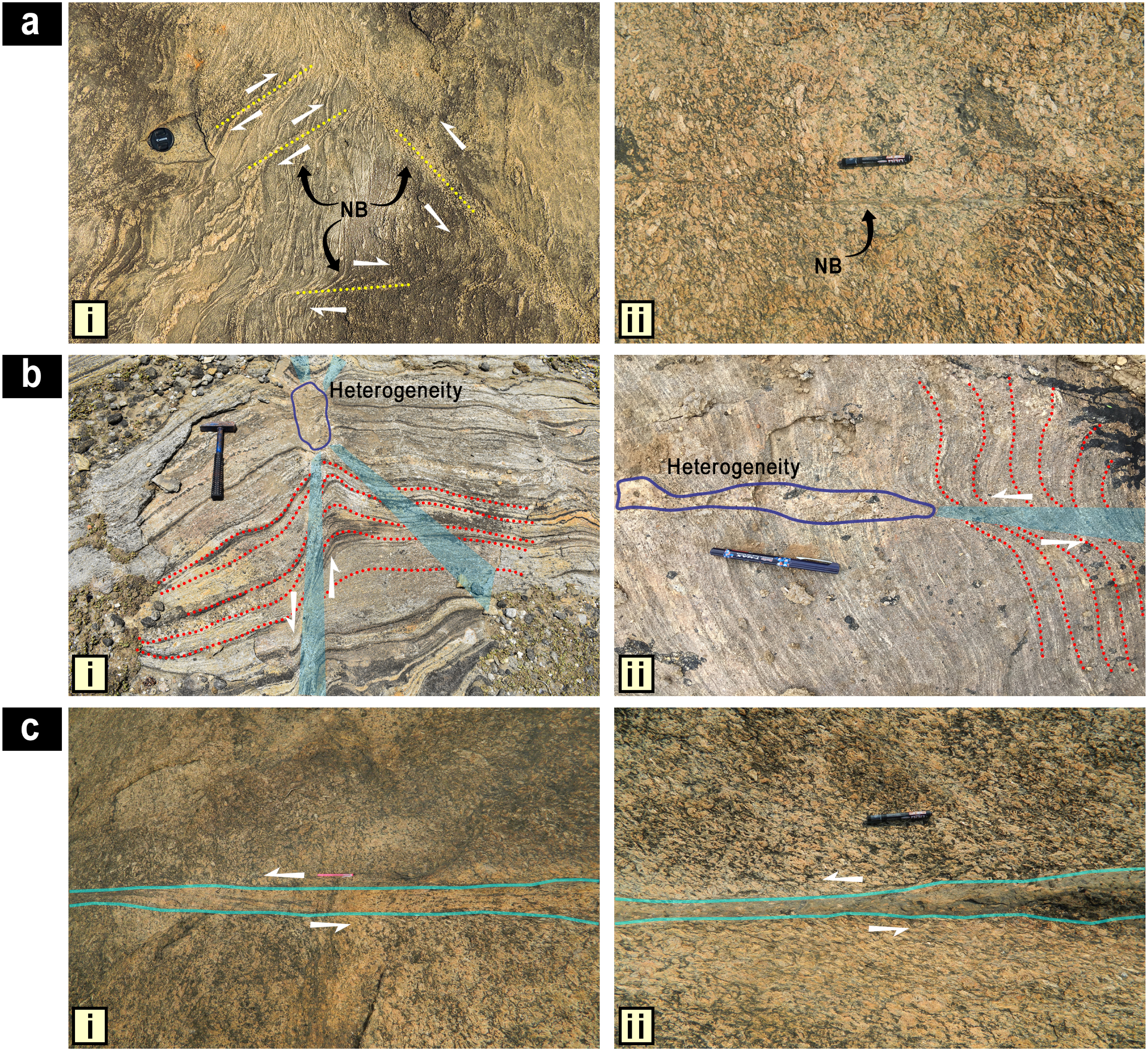

a
NB
i
NB
ii
b
Heterogeneity
i
Heterogeneity
ii
c
i
ii

Figure 9.

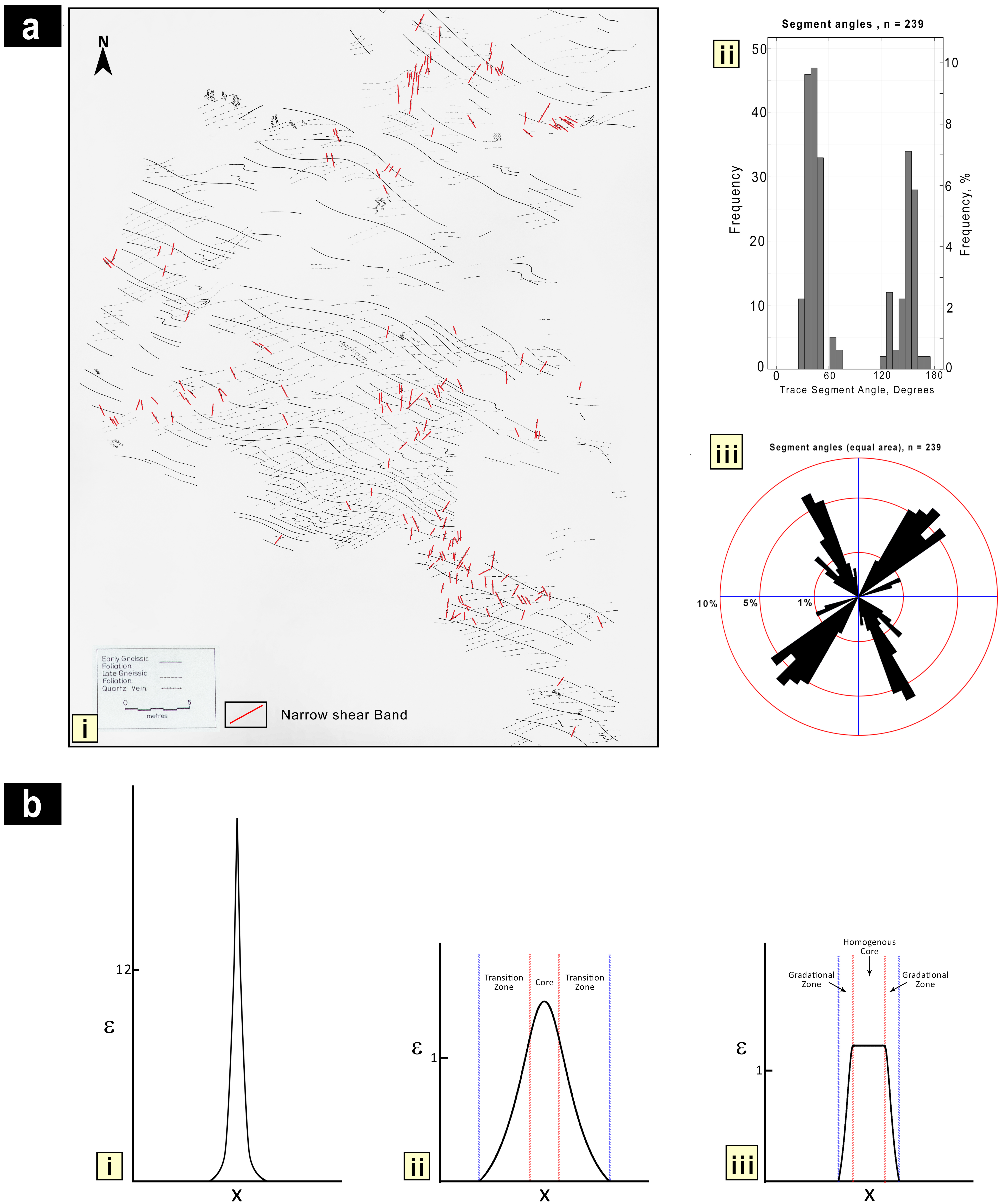

a
N
Early Gneissic Foliation.
Late Gneissic Foliation.
Quartz Vein.
0
5
metres
Narrow shear Band
i
ii
Segment angles , n = 239
50
40
30
20
10
0
Frequency
10
8
6
4
2
0
Frequency, %
0
60
120
180
Trace Segment Angle, Degrees
iii
Segment angles (equal area), n = 239
10%
5%
1%
b
i
12
ε
x
ii
ε
1
Transition Zone
Core
Transition Zone
x
iii
Homogenous Core
Gradational Zone
Gradational Zone
ε
1
x

Parameters	***Symbol***	***Natural Values***	***Numerical Input Values***
Model length	L	30 km	3
Model width	W	30 km	3
Model reference strain rate	$\dot{\gamma}_o$	$3.17e^{-14}$	1
Model reference density times gravitational acceleration	ρ g	27000 kg m^{-2} s^{-2}	8.52
Model reference viscosity	η_0	$1e^{21}$ Pas	1
Initial Cohesion	C_i	20 Mpa	0.63
Cohesion after Softening	C_s	5 Mpa	0.16
Angle of friction	ϕ	25° - 30°	25° - 30°
Maximum Yield stress	σ_{max}	1000 Mpa	31.56
Minimum Yield stress	σ_{min}	10 Mpa	0.32
Elastic shear module	G	5 x 10^9 Pa	157.78

Journal of Geophysical Research: Solid Earth

Supporting Information for

Mechanisms of shear band formation in heterogeneous materials under compression: The role of pre-existing mechanical flaws

Manaska Mukhopadhyay, Arnab Roy and Nibir Mandal*

High Pressure and Temperature Laboratory, Department of Geological Sciences, Jadavpur University, Kolkata 700032, India.

Contents of this file

S1. Comparison of physical properties between Polystyrene and Granite at 500°C

A range of materials, such as synthetic granular solids, polymers and metals have been used as rock analogues to study crustal deformations in laboratory. For example, recent experiments used GRAM (a polymeric rock analogue) to investigate the development of shear bands under compression (Chemenda & Mas, 2016). We chose polystyrene, a commercial available polymer in our experiments. Interestingly, this material displayed deformation localization behaviour, as shown from GRAM. The following sections present a rheological comparison of polystyrene with common crustal rocks.

Yield point versus Young's modulus ratio:

The PS was chosen as an effective rock analogue material based on the rheological equivalence, as required in this kind of experiments. To demonstrate this, we compared the stress versus strain relations of PS with that of granite, which commonly represent the crust. Yield point is one of the most fundamental property of a rock that defines the critical stress at which it plastically yields to deform permanently. Similarly, Young's modulus, the measure of stiffness of an elastic material, is another crucial physical property to determine the pre-yield elastic deformation. To establish our choice of PS as the rock analogue material, we calculated the ratio between yield point and the young's modulus of our material and compared with some classical experimental data given by previous workers (Table S1). As we are considering a depth of upper-mid crustal rocks, we took the yield behaviour of granite at 500°C as our reference.

Author	**Yield Point : Young's Modulus**
Griggs et al., 1960	0.025
Tulis and Yund, 1977	0.027
Jaeger and Cook, 1979 & Ranalli, 1995	0.033
Our Model Material (PS)	*0.035*

Table S1: Comparison of yield point : young's modulus of granite with polystyrene

Poissons' Ratio:

Similar to yield point and young's modulus, Poisson's ratio is another important parameter that governs the elastic property of a material. To establish our choice of polystyrene as model material, we have compared the Poisson's ratio of commonly found upper-mid crustal rocks with Polystyrene (Table S2).

Material type	**Poisson's Ratio**
Granite	0.2-0.3
Marble	0.2-0.3
Quartzite	0.23
Polysterene	*0.34*

Table S2: Comparison of Poisson's ratio of crustal rocks with polystyrene

Dihedral Angle of Shear Bands:

Griggs et al. (1960) showed deformation of rocks at 500°C to 800°C. In their study, they showed shear bands developing in granite at high temperature (in the plastic creep regime)

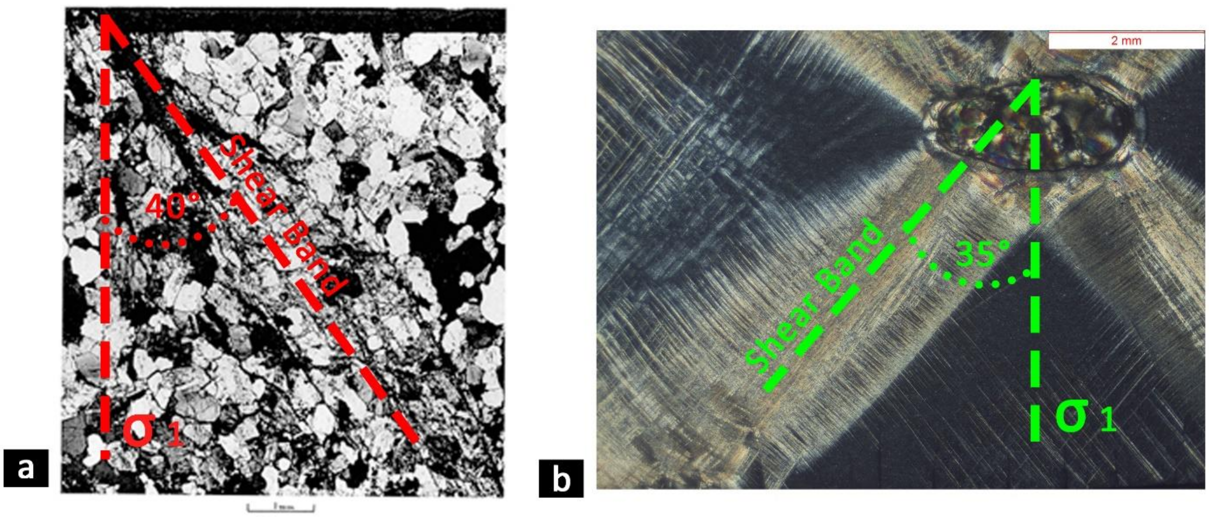

Fig. S1: a) Dihedral angle of granite at high temperature (after *Griggs et al., 1960*); b) Dihedral angle of polystyrene at room temperature

with a dihedral angle of ~80°. This value closely resembles with the dihedral angle of composite bands (~75°) formed in our PS models with heterogeneities, as shown in the Figure S1.

Strain-rate sensitivity

The PS material chosen in the present experiments was sensitive to strain rate, showing a spectacular transition in the mode of shear localization (homogeneous to composite band formation) on a small range ($2x10^{-5}$ s^{-1} to $3x10^{-5}$ s^{-1}) of strain-rate variation in laboratory. We thus varied the strain rate in this narrow range in our experiments with heterogeneous PS models. Previous experimental studies (e.g., Bowden and Raha, 1970) also suggest that the mechanisms (micro- versus diffuse) of shear band formation can transform at some threshold strain rates. This strain-rate sensitivity of PS allows us to explore the effect of strain rate variations in geological conditions, e.g., 10^{-12} s^{-1} to 10^{-14} s^{-1}, as commonly reported in literature (Fagereng & Biggs, 2019; Pfiffner & Ramsay, 1982).

S2. Birefringence in deformed polymers

PS in its completely amorphous state is characterized by randomly oriented polymer molecular chains, and shows optically isotropic behavior (Fig. S2). The material

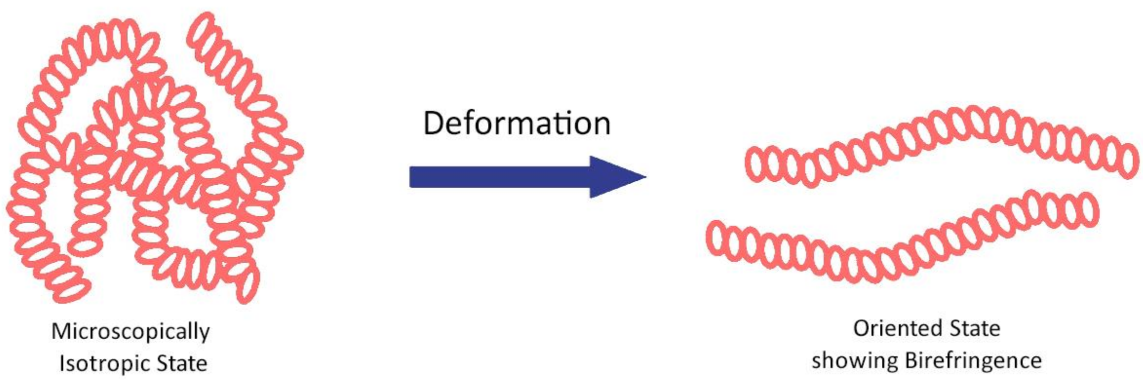

Fig. S2: a) Schematic diagram showing generation of birefringence due to deformation in polymers (after *Tagaya, 2013*).

in an undeformed condition is thus devoid of any birefringence. However, under stressed conditions, the randomly oriented polymer chains are aligned in a preferred direction, and such directionality in chain structures gives rise to anisotropic properties, as reflected in optical birefringence (Tagaya, 2013). The magnitude of birefringence holds a good correlation with the amount of plastic strain accumulation that determines the degree of molecular chain orientations. The deformation induced birefringence is irreversible as it develops in response to permanent strains in the material. We could thus qualitatively use this birefringence property to delineate the zones of permanent strain localization in deformed PS blocks.

S3. Homogeneous model experiments at lower strain rate

We performed an additional set of experiments to test the sensitivity of homogenous PS blocks to strain rate in forming shear band structures (Fig. S3). The experiments were run at a lower strain rate, 3 x 10^{-5} s^{-1} to 2 x 10^{-5} s^{-1}, as compared to those presented in the main text (Fig. 3a). This range of strain rates produced sharp and narrow bands that are finely spaced and uniformly distributed in the entire model. They typically formed in conjugate sets, symmetrically oriented with respect to the compression direction. The bands multiplied in number with increasing finite strain, as observed in similar

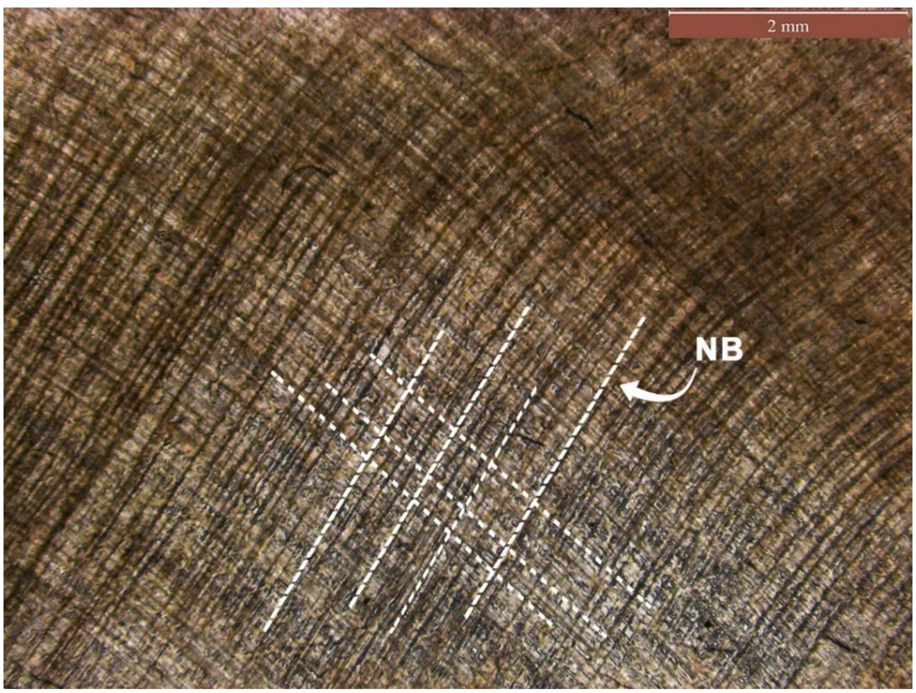

Fig. S3: Uniform development of closely spaced, conjugate narrow bands in homogenous PS models deformed at low strain rate ($\dot{\varepsilon} = 2 \text{ x } 10^{-5}\ s^{-1}$). Note that strain rate doesn't have any effect on shear band formation in homogeneous model.

experiments at relatively higher rates, and they had no tendency to widen, but grow in length. The PS produced distributed narrow bands in its homogeneous state under the entire range of strain rate conditions used in our laboratory experiments. We thus conclude that uniformly thick bands of homogeneous shear in low-strain rate experiments reflect the influence of weak flaws in the model.

S4. Experimental result of heterogeneous model with a single hole

An additional set of compression experiments was performed on polystyrene blocks containing single flaws in the middle of the model. The flaw diameter was kept 1mm, similar to the experiments with multiple flaws. The experiments were conducted at room temperature under strain rates similar to the previous ones. The single-flaw models

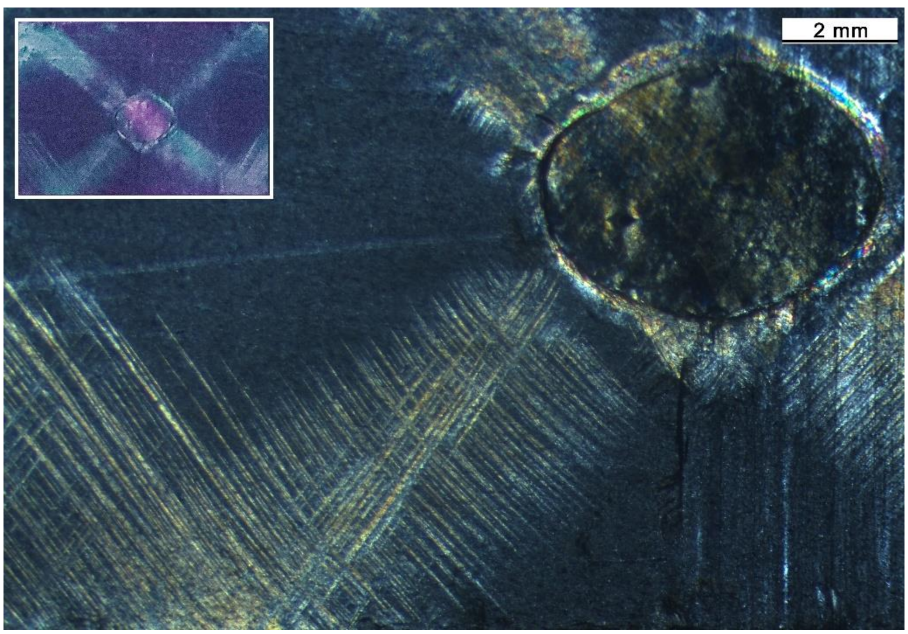

Fig S4: Development of shear band patterns in a single-flaw polystyrene model. The full view of bands around the flaw is shown in the inset. Note that the composite band geometry and its internal band structure are identical to that produced in a model containing a pair of flaws. The single-flaw experiments confirm that there were no mutual interactions between flaws in the experiments presented in the main text.

produced a pattern exactly similar to those observed in experiments containing two flaws (Fig. S4). The single-flaw experiments clearly reveal the absence of any mutual interaction between the flaws in the two-flaw experiments. The weak heterogeneities considered in our experimental modelling acted as a single mechanical entity in the mechanics of shear band localization.

S5. Calculation of finite strain

Let $\acute{\alpha}$, $\acute{\beta}$, be the angle formed by the passive marker with shear zone and shear band boundary respectively. Also, $2y_1$ and $2y_2$ are the shear zone and shear band thickness

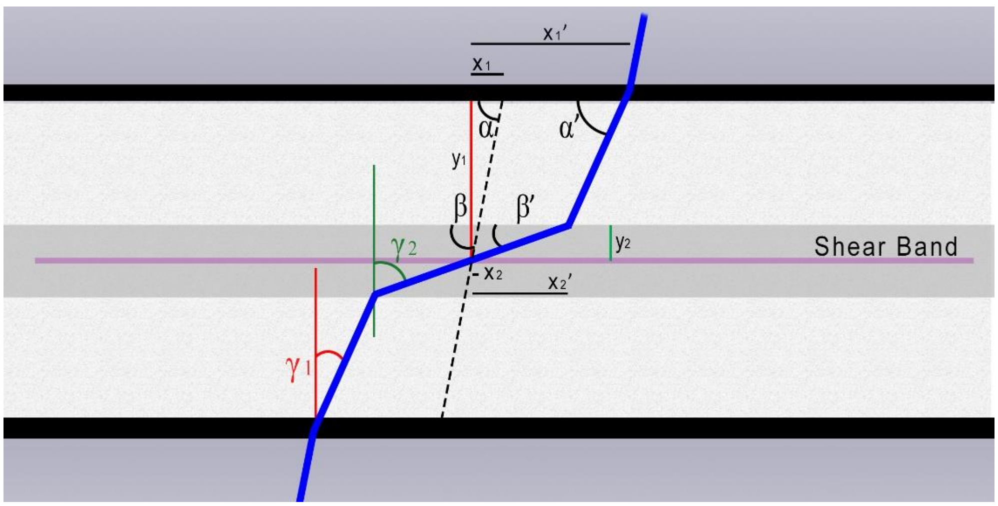

Fig. S5: Schematic representation of finite strain measurement using a passive marker (blue line).

respectively. Let γ be the total finite strain. We know that,

$$\gamma = \gamma_1 + \gamma_2 \qquad \text{(S1)}$$

From Fig S5,

$$\acute{x}_1 = x_1 + \gamma_1 y_1 \qquad \text{(S2)}$$

Dividing both side by y, we get

$$\frac{\acute{x}_1}{y_1} = \frac{x_1}{y_1} + \gamma_1 \qquad \text{(S3)}$$

$$\cot \acute{\alpha} = \cot \alpha + \gamma_1 \qquad \text{(S4)}$$

Similarly, from Fig. S5,

$$\frac{\acute{x}_2}{y_2} = \frac{x_2}{y_2} + \gamma_2 \qquad \text{(S5)}$$

$$\cot \acute{\beta} = \cot \beta + \gamma_2 \qquad \text{(S6)}$$

We calculate the total finite strain using Eq. S1.

S6. Mesh refinement study

We performed a mesh refinement test to evaluate the sensitivity of band structures with varying mesh resolution sensitivity in our elasto-visco-plastic numerical models. The

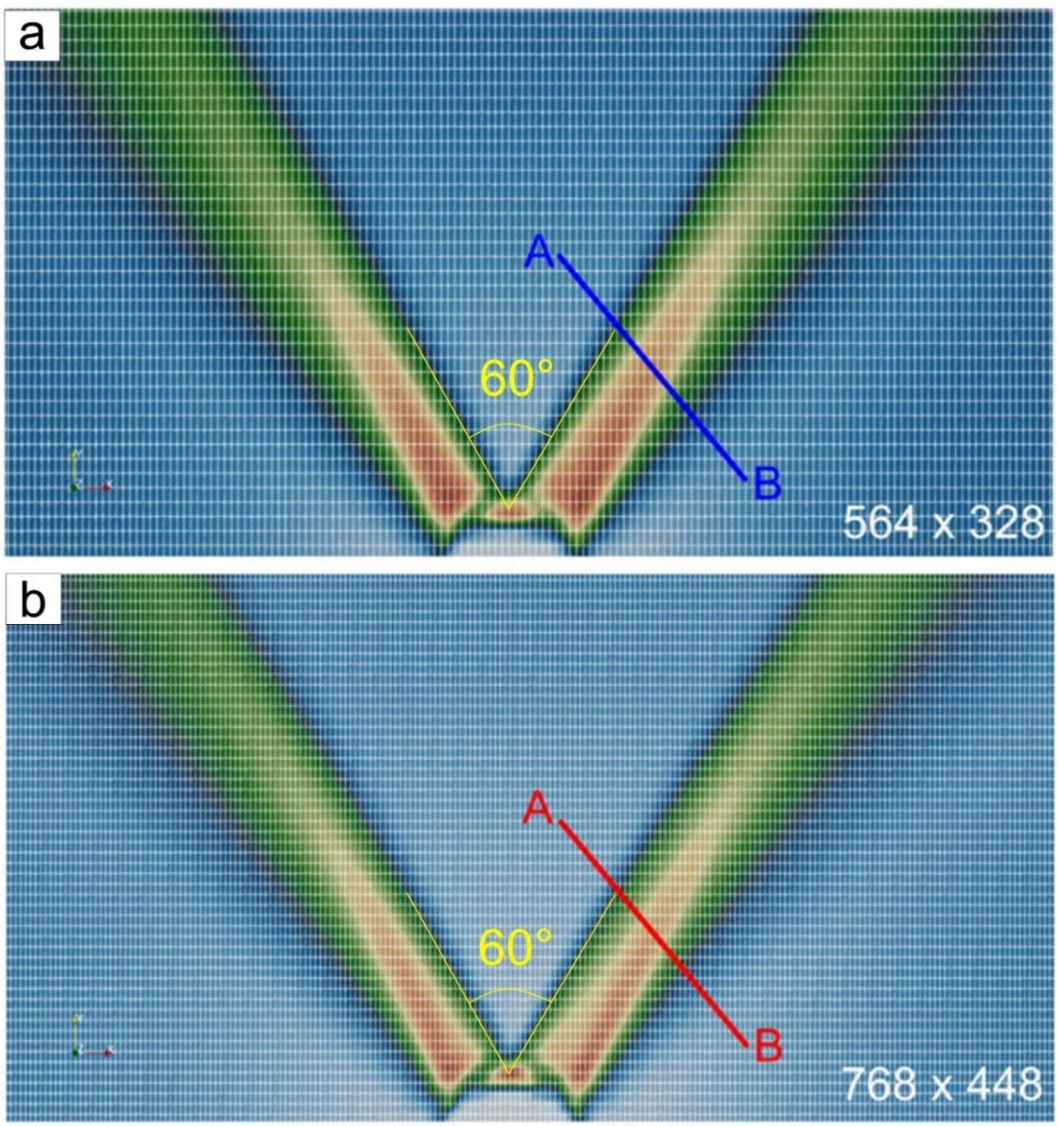

Fig. S6.1: Two numerical simulations run under the same conditions, but with different mesh resolution: a) 564x328 b) 768x448.

test revealed that the band structures hardly changed after attaining a fine resolution. For example, two simulations run under exactly the same conditions but with different mesh resolutions, 768x448 and 564x384, produce almost identical shear band structures with minute details (Fig. S6.1). The mesh resolution of 564x384 was thus chosen for all the simulation runs presented in this study. Earlier workers have also used the mesh resolution of the same order in their simulations (Duretz et al., 2019).

The two experiments show similar dihedral angle between the shear bands (60°) and similar pattern of the magnitude of accumulated strain along the profile AB (Fig. S6.2) across the shear bands.

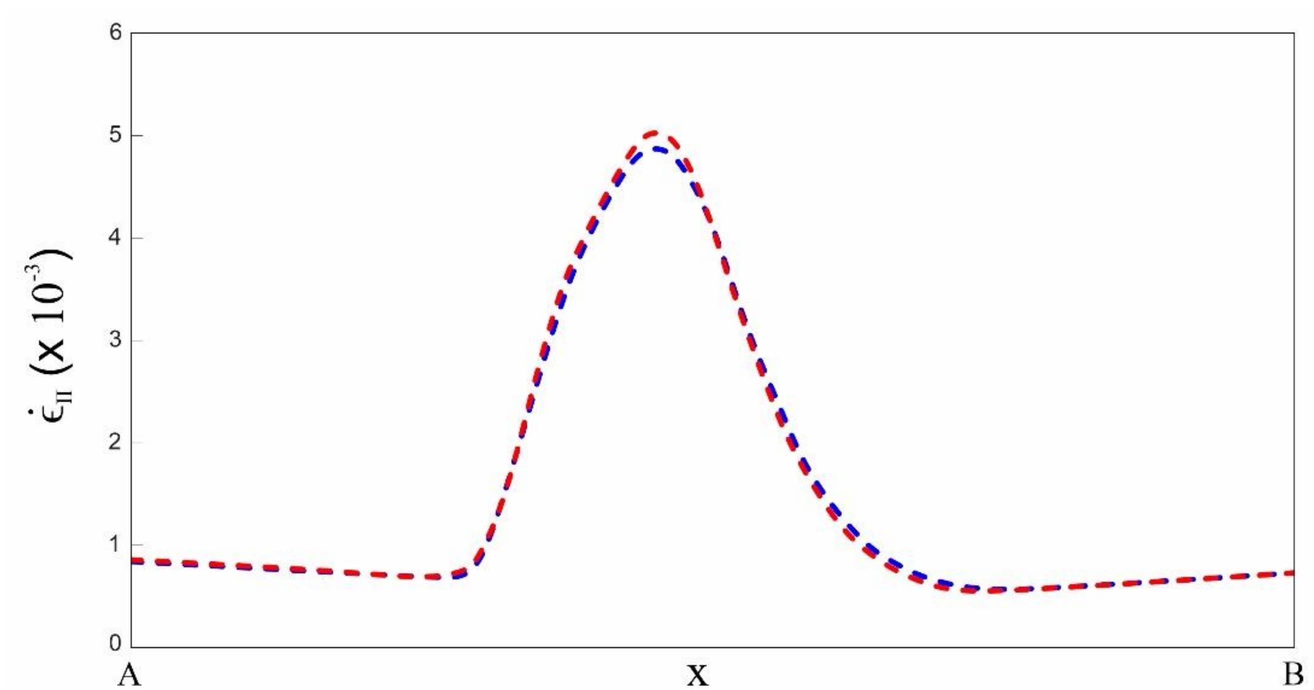

Fig S6.2: Profiles of accumulated strain probed across the shear bands of two different set of numerical simulation with resolution 564x328 (blue line) and 768x448 (red line).

S7. Across-band strain profiles in numerical models

This section discusses the strain profiles calculated from the numerical simulation MS2 run at relatively high rates (results presented in the main text). The profiles are constructed along the lines AB, CD, EF, as shown in Figure 6 in the main text. They represent plots of the 2nd invariant of the strain rate tensor (sum of the elastic, viscous and plastic strain components) as a function of distance in the model. The strain profiles contain multiple peaks that reveal the composite nature of shear bands, as observed in the PS experiments at a high strain rate (3 x 10^{-5} s^{-1}).

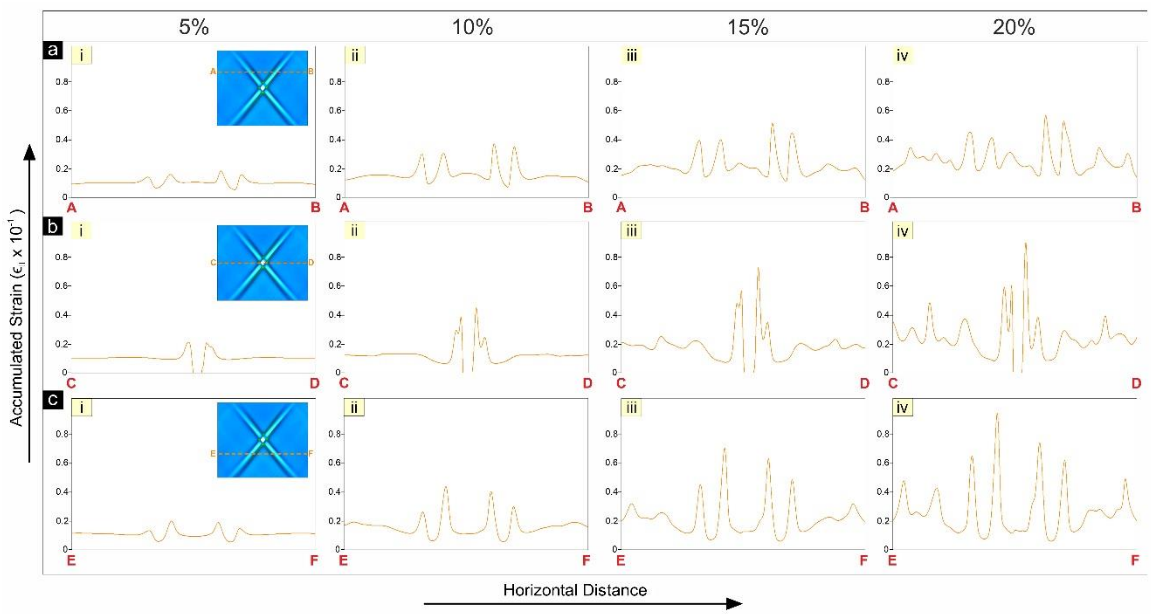

Fig S7: Across-band strain profiles in MS2 (locations of the profile lines: AB, CD, and EF, shown in inset). Note that the strain profiles show multiple peaks signifying the formation of multiple shear bands in the core zone.

S8. Field study of natural shear zones

We studied a few centimetres to tens of metres long ductile shear zones in the Chotanagpur Granite Gneissic Complex (CGGC), focusing upon regions north of the South Purulia Shear Zone (SPSZ). The shear zones are associated with alkali granite, brecciated quartzite, apatite-magnetite bearing chert, U-Th mineral-bearing pegmatite and mafic-ultramafic rocks. The host rock types include banded, porphyritic and augen granite gneisses, garnet-bearing quartzo-feldspathic gneisses, khondalite, amphibolites and mafic granulites, which generally contain penetrative tectonic foliations of single or multiple generations. The host foliations act as markers, showing sharp deflections across shear bands that allow us to identify the mode of shear localization. In places we could recognize mechanical heterogeneities as nucleating agents of shear zones. For example, high-temperature metamorphic rocks in the Jasidh area show band localization in the vicinity of quartzo-feldspathic aggregates, which possibly represent melt lenses (weak zones) produced by partial melting during the granulite facies metamorphism. This kind of field examples support our experimental interpretation that mechanically weak heterogeneities can be a crucial factor for the formation of isolated shear zones in continua.

We chose three prominent locations: 1) Bero Hillocks (23°32'09.5" N, 86°40'01.3" E) near Raghunathpur town, 2) Purulia-Asansol Road transect near Baraseni (23°25'20.9"N 86°28'48.8"E), and 3) Jasidih (24° 31′ 19.2″ N, 86° 38′ 51.72″ E) (Fig S8). Location 1 is predominantly composed of biotitic granite gneiss, which shows excellent shear band structures with thick strongly shear core, sometimes flanked by excellent drag zones on both sides, while some shows relatively weakly deformed matrix. Lithologically, Location 2 is a fine-grained granulite-facies rock, primarily composed of alkali-feldspar, with minor amounts of quartz, mica, garnet and tourmaline. Classically this rock type is also termed as Leptynite and they often show a planar gneissic structure. Location 2 exhibits extensive micro shear band structures with a cross cutting relationship throughout the exposure (Fig. 8 a). Location 3 is situated near the Jasidih area, which lies in the northernmost part of CGGC. Lithologically, this area is predominantly of migmatitic felsic orthogneiss origin, with random enclaves of meta -sedimentary and meta-mafic rocks. We found excellent shear bands occurring in the vicinity of elliptical to semi-elliptical heterogenous clasts (Fig 8b), that can be well correlated with our heterogenous models (Fig. 3 b).

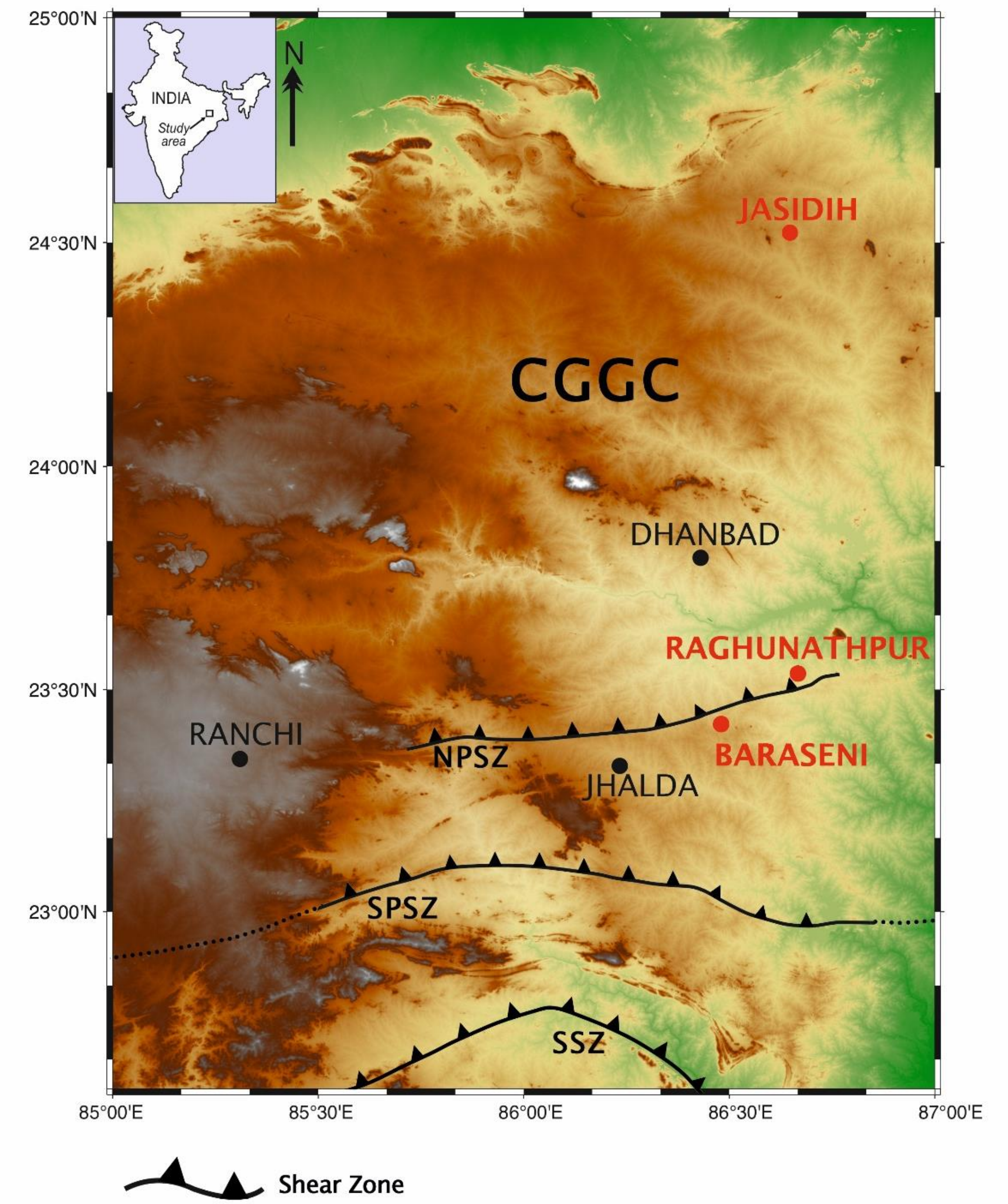

Fig. S8: A simplified geological map of the East Indian Precambrian craton, showing the locations of the Singhbhum Shear Zone (SSZ), the South Purulia Shear Zone (SPSZ), the North Purulia Shear Zone (NPSZ) and the Chotanagpur Granite Gniess Complex (CGGC). Field areas are marked by red dots in the map.

S9. Strain profiles from field studies

This section presents the strain profiles obtained from strain analyses performed in field outcrops. Strain profiles were obtained by calculating the finite strain (ε) across various types of shear zones. Type I shear zones containing narrow shear bands observed in an area near Purulia town, showed a characteristic curve with a high peak showing large ε values implying intense shear localisation across the narrow shear bands (Fig 9b-i). Type II shear zones showed gradational shear strain variation from weakly deformed wall to highly sheared core forming a typical bell-shaped curve (Fig 9b-ii). On the contrary, Type III shear zones are characterized by a plateau like strain profile with very narrow gradational zone (Fig 9b-iii). This characteristic shape results due to formation of a very narrow drag zone on both sides of the homogenous core zone.

References:

Chemenda, A. I., & Mas, D. (2016). Dependence of rock properties on the Lode angle: Experimental data, constitutive model, and bifurcation analysis. *Journal of the Mechanics and Physics of Solids*, *96*, 477–496. https://doi.org/10.1016/j.jmps.2016.08.004

Duretz, T., de Borst, R., & Le Pourhiet, L. (2019). Finite Thickness of Shear Bands in Frictional Viscoplasticity and Implications for Lithosphere Dynamics. *Geochemistry, Geophysics, Geosystems*, *20*(11), 5598–5616. https://doi.org/10.1029/2019GC008531

Fagereng, Å., & Biggs, J. (2019). New perspectives on 'geological strain rates' calculated from both naturally deformed and actively deforming rocks. *Journal of Structural Geology*, *125*(October 2018), 100–110. https://doi.org/10.1016/j.jsg.2018.10.004

Pfiffner, O. a, & Ramsay, J. G. (1982). Conventional Strain. *Journal of Geophysical Research B: Solid Earth*, *87*(B1), 311–321.

Tagaya, A. (2013). Encyclopedia of Polymeric Nanomaterials. *Encyclopedia of Polymeric Nanomaterials*, 1–6. https://doi.org/10.1007/978-3-642-36199-9